THESIS

# EVIDENCE FOR FLUID-ASSISTED SHEAR FAILURE IN A DUCTILE SHEAR ZONE: TECTONIC TREMOR IN THE GEOLOGIC RECORD?

Submitted by

Katharine Compton

Department of Geosciences

In partial fulfillment of the requirements

For the Degree of Master of Science

Colorado State University

Fort Collins, Colorado

Summer 2015

Master's Committee:

Advisor: James Kirkpatrick

Jerry F. Magloughlin
Joe von Fischer

Copyright by Katharine Elizabeth Compton 2015

All Rights Reserved

ABSTRACT

EVIDENCE FOR FLUID-ASSISTED SHEAR FAILURE IN A DUCTILE SHEAR ZONE: TECTONIC TREMOR IN THE GEOLOGIC RECORD?

Recent direct observations of tectonic tremor below the seismogenic zone of large fault zones have emphasized the significance of coeval ductile and brittle processes at high temperatures. Tectonic tremor is defined as long-duration, low-amplitude, and low-frequency seismic signals produced at depths of 18-40 km. Because the source of tremor is currently unknown, the physical conditions and processes that cause tremor are unknown. This study presents observations of an exhumed shear zone system contained within the Saddlebag Lake pendant of the eastern Sierra Nevada, California. The high-strain rocks in this shear zone exhibit multiple episodes of vein formation, indicating a prolonged migration of hydrothermal fluids through the system. Crosscutting relationships and mineral assemblages define discrete sets of variously oriented veins that are folded and boudinaged. I document foliation-parallel quartz veins that show shear displacement parallel to the foliation. Textural evidence for dynamic recrystallization mechanisms, stable isotope data, and fluid inclusion thermobarometry measurements indicate temperatures between 300-680°C and relatively high fluid pressure conditions, greater than $\sigma_3$, during fracture. Conditions of nucleation of shear fractures within this ductile shear zone suggest these structures may record similar processes to those under which tectonic tremor is observed in other continental transform fault zones. I interpret that these veins formed as shear fractures under increasing differential stress and fluctuations in pore pressure, with failure driven by heterogeneous materials within the shear zone.

ACKNOWLEDGEMENTS

First and foremost, I would like to thank my graduate advisor, Dr. James Kirkpatrick, for his unending patience and intellectual input into this project. I would like to thank Dr. Scott Paterson for introducing us to this study area, Yosemite National Park for the permission to work in the area and collect samples, and my field assistants, Lloyd Augustus (Gus) Womeldorph and Kate Shervais, for their moral and physical support. I would also like to extend my gratitude to Dr. Gregory Holk of California State University Long Beach for his time and effort both in the lab and writing processes, Dr. John Ridley of Colorado State University for his instruction and aid regarding fluid inclusion thermobarometry, and Dr. Roy Geiss of Colorado State University for his patience and knowledge regarding our electron backscatter diffraction work. Lastly, I would like to thank my committee members, Jerry Magloughlin and Joe von Fischer, for dedicating the time to reviewing and considering my thesis. I am very grateful for the time and consideration each of you has invested in this project. Additional thanks to the department of Geosciences for supporting and funding for this project.

TABLE OF CONTENTS

ABSTRACT ..... ii

ACKNOWLEDGEMENTS ..... iii

CHAPTER 1: INTRODUCTION ..... 1

CHAPTER 2: EVIDENCE FOR FLUID-ASSISTED SHEAR FAILURE IN A DUCTILE SHEAR ZONE: TECTONIC TREMOR IN THE ROCK RECORD? ..... 6

2.1 INTRODUCTION ..... 6
2.2 TREMOR IN THE ROCK RECORD ..... 8
2.3 GEOLOGIC SETTING ..... 12
2.4 FIELD AND MICROSTRUCTURAL OBSERVATIONS ..... 15
2.5 STABLE ISOTOPE GEOCHEMISTRY ..... 26
2.6 INTERPRETATION ..... 28
2.7 DISCUSSION ..... 33
2.8 CONCLUSION ..... 39

TABLES ..... 41

FIGURES ..... 42

CHAPTER 3: FUTURE WORK ..... 58

REFERENCES ..... 60

APPENDIX A: EXPOSURE MAPS ..... 68

APPENDIX B: FLUID INCLUSION THERMOBAROMETRY ..... 71

APPENDIX C: TOURMALINE VEIN MOSAIC ..... 75

# CHAPTER 1: INTRODUCTION

Tectonic tremor, defined as a long-duration, low-amplitude and low-frequency seismic signal, was originally recognized on the Nankai subduction zone in 2002 (Obara, 2002). Tremor is found in large subduction zones and along continental transform faults, such as the San Andreas Fault in California and the Alpine Fault in New Zealand (Rogers and Dragert, 2003; McClausland *et al.*, 2005; Zhang *et al.*, 2011; Chamberlain and Shelly, 2014). Additionally, tremor has been recognized in Taiwan, Cuba, and western Canada (Peng and Chao, 2008; Aiken *et al*., 2012; Chao *et al.*, 201). The seismic signal of tremor is indistinct, similar to noise, but contains stacked signals of multiple low- or very- low frequency earthquakes (LFE/VLFE), which have average frequencies of 1 Hz and 0.02-0.05 Hz, respectively (Burlini *et al.*, 2009; Wech *et al*., 2012). Tectonic tremor lasts between minutes and days in length. These VLFE's have distinctive P and S body wave arrival times, which are used to both locate tremor and indicate that it is caused by shear failure on the plate interface. Elevated fluid pressures have been suggested as a mechanism driving the shear failure that is tectonic tremor, as it is most commonly found near subduction zones with associated dehydrating slabs (Obara, 2006; Obara *et al.*, 2006), and is also observed where geophysical data provide an independent constraint on the fluid pressure (Wech *et al.*, 2012). Tremor is recognized at depths of 18-40 km. For example, tremor depths along the San Andreas fault are shown in Figure 1. These depths, when applied to a geothermal gradient of 30°C/km (Williams *et al.*, 2004), correspond to temperatures of greater than 500°C (Shelly and Hardebeck, 2010). At these temperatures, rocks are expected to deform viscously by crystal plastic deformation as opposed to fracturing. Due to a virtually undetectable seismic signal, seismologists have not yet identified the cause of tectonic tremor. Further, the

low amplitude wave signals make estimating the location of tremor very difficult. Because the source parameters and exact locations of tremor remain poorly constrained, the physical mechanism causing fracture where viscous deformation should occur remains unknown.

One additional source of data that could contribute to the understanding of tremor is evidence from the geologic record. Brittle structures such as fluid-filled veins and pseudotachylyte are preserved in many shear zones. With slow slip and tremor in mind, researchers have provided models for the formation of shear fractures and vein systems in a system that is deforming dominantly by ductile deformation (Hobbs *et al.*, 1986; Hayman and Lavier, 2014; Fagereng, 2014). Veins in shear zones are common (Kerrich and Allison, 1978; Hodgson, 1987; Henderson and McCaig, 1996), with varying orientations thought to be a result of major stress re-orientations during deformation. To date, only three papers have attempted to relate structures in ancient systems to the seismologically observed tectonic tremor (Fagereng et al., 2011; Fagereng et al., 2014; Hayman and Lavier, 2014).

This project focuses on the kinds of evidence for shear failure present in a ductile systems, with two main goals in mind: 1) to describe the conditions and processes that cause shear fracture formation in a ductile system, and 2) to determine whether or not these structures have formed under similar conditions to tectonic tremor. Over the course of this investigation, I have used a number of specialized techniques to better understand the system. These techniques include field mapping, petrographic analysis of dynamically recrystallized quartz, fluid inclusion thermobarometry, stable isotope geochemistry, and electron backscatter diffraction.

In order to create accurate basemaps for field mapping, I used Agisoft Photoscan Pro, a computer program that uses stereogrammetry techniques to stitch together hundreds of photos to create a digital elevation model using the camera perspectives of each photo. A texture (color

map) is draped onto the model to provide an accurate representation of the surface. The resulting model was rotated to a horizontal exposure and exported, and used as an orthorectified basemap for field annotation using an iPad. These images allowed for accurate, detailed field maps to be created in a timely manner. More detailed, neater versions of these maps were made in the lab after fieldwork was completed using field annotations and measurements. Ground control points were taken with a real time kinematic (RTK) differential GPS system to accurately measure locations of outcrops and provide a physical scale to the models.

Samples of foliation-parallel quartz veins were studied for evidence of dynamic recrystallization to determine temperatures of ductile deformation. I compared microtextures of quartz in the veins to dynamic recrystallization mechanisms summarized by Passchier and Trouw (2005). In addition, I studied the metamorphic assemblages of the Triassic and Jurassic units within the shear zone to determine the metamorphic history of the rocks and their related temperatures.

Fluid inclusion thermobarometry was conducted to obtain homogenization and freezing temperatures of fluid inclusions. These temperatures indicate the temperatures at which fluid entered the system, and help constrain a thermal history. For detailed methodology, see Appendix B.

Oxygen and hydrogen isotope analysis was performed on four samples from one outcrop in order to obtain information regarding the fluid sources during deformation. Oxygen occurs as three oxygen isotopes, $^{16}O$ (light), $^{17}O$, $^{18}O$ (heavy); the relative amounts of these two isotopes are a function of the climate and environment. Oxygen isotope analysis works by analyzing the ratio of $^{18}O$ to $^{16}O$ in the samples. Resulting data are signified by $\delta^{18}O$ values. Hydrogen contains protium and deuterium; the deuterium levels are measured through the hydrogen isotope analysis

(signified by δD). A fractionation factor, determined by the temperature of mineral formation and the composition of the mineral, is applied to the raw data. I plotted these data against constrained values of magmatic and metamorphic water, as well as the specific $\delta^{18}O$ range for the nearby batholith.

Electron backscatter diffraction analysis was performed on dynamically recrystallized quartz veins to constrain an average grain size and orientation patterns of grains across individual samples. This technique takes a standard geologic thin section coated with carbon to the scanning electron microscope, where the sample is then tilted to an angle of 70 degrees relative to the horizontal. A beam of electrons is fired at the sample, and the patterns of electron diffraction from the sample are a function of the orientation of the crystal lattice. The resulting patterns are evaluated for deformation temperature and average grain size. The grain sizes measured can be applied to empirically derived paleopiezometry methods to estimate a flow stress (Stipp and Tullis, 2003). In order to expedite the index calibration process, a piece of silicon was attached to the sample holder with copper tape. Because quartz is comprised of silicon and oxygen, the silicon was then indexed in the Optical Imaging Microscopy (OIM) software and used to calibrate the program.

This thesis is formatted with the intention of submitting it for publication to a journal. Section 2.2 introduces tectonic tremor, introducing observed seismic characteristics of tectonic tremor from the literature, and presents the current ‘unknowns’ in the study of tremor. Using the observed characteristics, I discuss physical structures I could expect to correspond to tremor in the geologic record. Section 2.3 introduces the study area, describing the geologic history of the Sierra Nevada and the specific roof pendant and shear zone of this study. This section also introduces rock units and deformation history of the shear zone. Section 2.4 presents the field

and microstructural observations of this project. This includes both outcrop- and grain- scale observations. In this section, I present structural data and describe both the large- scale deformation of the shear zone and the petrology of the three main rock units. I describe the multiple sets of veins in this shear zone, providing my observations of their structural natures and relationships. I provide descriptions of dynamically recrystallized quartz grains and of two sets of fluid inclusion trails, and present quantitative data for the latter. Lastly, I describe the results from the electron backscatter diffraction work, providing constraints on grain size distribution of recrystallized grains. Section 2.5 describes the stable isotope results. I provide methodology for sample preparation as well as my results, comparing my data to accepted data ranges for the Sierra Nevada region and the nearby Tuolumne Intrusive Complex. Section 2.6 serves as the interpretation of all of the above-mentioned data. Section 2.7, the discussion, compares data from this study to previously published models of similar structures. This section also compares data in this study to the characteristics of tectonic tremor explained in Section 2.2, with the goal of comparing the structures and tremor. Chapter 3 gives suggestions for future work.

# CHAPTER 2: EVIDENCE FOR FLUID-ASSISTED SHEAR FAILURE IN A DUCTILE SHEAR ZONE: TECTONIC TREMOR IN THE ROCK RECORD?

## 2.1 Introduction

Tectonic tremors are low-amplitude, long-duration seismic signals observed to occur at major subduction zones and continental transform faults around the world (Rogers and Dragert, 2003; McClausland *et al.*, 2005; Zhang *et al.*, 2011; Aiken *et al.*, 2013; Chamberlain and Shelly, 2014). Careful observation of low and very low frequency earthquake signals embedded within tremor bursts indicates a lag between the peak arrival times of P and S body waves, indicating tremor occurs by shear failure at depth (Shelly *et al.*, 2007; Rocca *et al.*, 2009). Multiple characteristics of tectonic tremor have been constrained from detailed waveform analysis, including hypocentral depths, locations, frequencies, and stress drops (e.g. Shelly, 2009; Rubinstein *et al.*, 2010; Shelly and Hardebeck, 2010; Fletcher and McGarr, 2011). However, since tremor signals themselves lack distinctive body waves, the source mechanism remains enigmatic.

Seismic observations indicate a source depth of 18-40 km for tectonic tremor in subduction zones and transform fault environments (Rogers and Dragert, 2003; Shelly and Hardebeck, 2010). These depths are sufficient that elevated temperatures would promote crystal-plastic deformation, and therefore shear zones at these depths may be expected to deform predominantly by steady-state creep (Stipp *et al.*, 2003). Previously published geological observations and mechanical models explaining the cause of shear failures in tremor environments are primarily focused on portions of ancient subduction zones (Fagereng *et al.*, 2011; Hayman and Lavier, 2014; Fagereng *et al.*, 2014). These previous studies focused on

interpreting the formation of brittle fractures in environments predominantly deforming via viscous deformation, emphasizing that the seismic characteristics of low frequency earthquakes can be associated with structures in exhumed systems. However, there are no studies from transform fault environments. Field observations of ancient structures exposed at the surface today in a transform fault setting may similarly help explain the conditions facilitating the nucleation of brittle fractures at depths consistent with crystal-plastic deformation.

Brittle structures such as mineralized fractures (veins) and rocks such as pseudotachylytes are observed within exhumed shear zones. Complex brittle and ductile cross-cutting vein systems have been observed in multiple shear zones, attesting to cyclical, or repetitive changes in rheology. Past research has attributed variations in vein orientation to stress cycling and stress-reorientations following earthquake rupture, interpreting the veins to form as extension fractures (Kerrich and Allison, 1978; Hodgson, 1987; Henderson and McCaig, 1996). Fluid-driven changes in the shear strength of rocks suggest high fluid pressures may cause the nucleation of earthquakes at the base of the seismogenic zone (Micklethwaite and Cox, 2004).

In this study, I focus on brittle structures that formed in a shear zone that deformed primarily via crystal-plastic deformation in order to 1) constrain the conditions of the formation of these structures and interpret the mechanical cause of fracture formation, and 2) compare the structures and their attributes to those of tectonic tremor. To accomplish the first goal, microstructures, fluid inclusions, and stable isotope data were collected from samples in the Steelhead lake shear zone. In order to explain the mechanics of fracture formation, I compare the observed conditions to previous mechanical models. These observations emphasize the importance of both high fluid pressure and mechanical heterogeneity in transitional behavior. Based on field and microstructural observations, I suggest the structures in this system are

comparable to structures observed by Hobbs *et al.* (1986), Hayman and Lavier (2014), and Fagereng (2014). To accomplish my second goal, results from this study are compared to interpretations to known conditions of tectonic tremor from literature, establishing characteristics that are consistent between these structures and tectonic tremor.

## 2.2 Tremor in the rock record

The seismic signal of tectonic tremor was first recognized on the Nankai subduction zone (Obara, 2002), and has subsequently been identified at a variety of other plate boundary faults, including transform faults (Rogers and Dragert, 2003; McClausland *et al.*, 2005; Zhang *et al.*, 2011; Chamberlain and Shelly, 2014). Tremor is defined by long duration, low amplitude seismic signals in the frequency range of 1-10 Hz that are distinct from earthquakes because they typically do not contain impulsive waveforms (Obara *et al*. 2004; Rubinstein *et al*., 2010). *Rogers and Dragert* (2003) originally coined the term episodic tremor and slip (ETS) to describe associated tremor and slow slip phenomena, the latter of which is defined as geodetically-resolved slow slip producing aseismic transients (Obara *et al.*, 2004; Peng and Gomberg, 2010; Skarbek *et al.*, 2012). Temporal and spatial relationships of tectonic tremor and slow slip led to the belief that the two concepts were related; however, later observation of each process independent of the other signifies a distinction between the two (Obara *et al*., 2006; Ito *et al*., 2007; Peng and Gomberg, 2010; Beroza and Ide, 2011).

Seismic signals with source durations ranging from less than one second to a few tens of seconds and frequencies from 0.02 - 10 Hz have been classified as low-frequency earthquakes (LFEs) and very low-frequency earthquakes (VLFEs). LFE frequencies range from ~1-10 Hz, and VLFE signals have associated frequencies of ~0.02 - 0.05 Hz (Burlini *et al.*, 2009; Wech *et*

*al*., 2012). Distinct LFE waveforms have been used to show that there are multiple LFE and VLFE signals within tremor bursts (Shelly *et al.*, 2007; Peng and Gomberg 2010; Beroza and Ide, 2011). While S waves can sometimes be identified on seismograms, P waves can only be recognized from stacked seismograms of repeated events. Observation of these body waves indicates a distinct lag in the peak arrival times of P and S waves, reflecting a double-couple shear failure event at depth (Shelly *et al.*, 2007; Rocca *et al.*, 2009).

Tectonic tremor has some unique properties compared to normal earthquakes. Tremor signals can exhibit either constant amplitude or bursts of many events with amplitudes higher than the background signal (Rubinstein *et al*., 2010; Beroza and Ide, 2011). Observations of tremor bursts suggest tremor occurs in a regular, predictable cycle in highly repeatable locations. (Rogers and Dragert, 2003; McCausland *et al.*, 2005; Shelley, 2015). Tremor bursts triggered by teleseismic waves from distant earthquakes and earth tides show that only small stress changes are necessary to initiate slip (Rubinstein *et al*., 2007; Thomas *et al*., 2009; Rubinstein *et al*., 2010; Beroza and Ide, 2011). This is consistent with failure at low effective stresses due to high pore pressures. Low stress drops, typically estimated in the range of 0.001-0.04 MPa, are thought to be characteristic for VLFEs embedded within tremor signals (Ito and Obara, 2006; Fletcher and McGarr, 2011).

Tremor has been observed in Shikoku, Japan (Shelly *et al*. 2006; Matzuzawa, 2009) and the Cascadia subduction zone (Rogers and Dragert, 2008; Rocca *et al.*, 2009; Zhang *et al.*, 2011). Additionally, it has been discovered along large continental strike-slip faults, most notably the transpressional Alpine Fault in New Zealand (Wech *et al*. 2012; Chamberlain and Shelly, 2014) and the San Andreas Fault in central California (Shelly, 2007; Rubinstein, 2007; Shelly and Hardebeck, 2010; Rubinstein, 2010, Fletcher and McGarr, 2011). Further, tremor was recently

located along the Queen Charlotte Margin, a transform fault off the coast of western Canada (Aiken *et al*., 2012), beneath the Central Range in Taiwan, an arc-continent collision tectonic environment (Peng and Chao, 2008), and along the left-lateral Oriente fault zone near Cuba, between the North American and Caribbean plates (Chao *et al.*, 2013).

In this study, I focus on structures that form in a ductile shear zone in a transform fault setting. Tremor signals along transform faults are observed at depths between ~18 and 40 km, suggesting failure occurs within the mid- to lower-crust or upper mantle (e.g. Shelly and Hardebeck, 2010, Wech *et al*., 2012). These depths are below the seismogenic zone, and are consistent with temperatures from 500-1000°C (calculated with a 30°C/km geothermal gradient). At these temperatures, thermally activated crystal-plastic deformation is expected to be important for quartzofeldspathic rocks (Brace and Kohlstedt, 1980).

The mechanical causes of brittle failure (LFE and VLFE) within the crystal-plastic regime and the nature of the resulting structures that could represent tremor events in the rock record are not entirely understood. *Hayman and Lavier* (2014) proposed that tremor is generated through combined fracture and viscous flow within mechanically heterogeneous ductile shear zones. Changes in velocity-weakening and velocity-strengthening frictional parameters resulting in geologic heterogeneities have also been invoked to explain the conditions under which tremor events could occur (Liu and Rice, 2005; Skarbek *et al.*, 2012). Recent work has suggested tremor bursts are recorded as mixed-mode fractures filled with minerals precipitated from hydrothermal fluids (Fagereng *et al*., 2011; Fagereng, 2014), consistent with the geophysical evidence for elevated fluid pressure at depth.

Few studies have related structures in shear zones to seismologically observed tremor (Fagereng *et al.*, 2014; Hayman and Lavier, 2014), so I used the seismic characteristics of

tectonic tremor on transform faults to attempt to predict what types of structures could represent individual LFEs or VLFEs in the rock record. As mentioned above, the temperatures at the source of tremor are relatively high, so if LFEs occur on a fault, the fault is likely to contain foliated mylonitic rocks that form by crystal plastic deformation mechanisms. If LFEs are caused by brittle shear failure, they would be recorded as fractures displaying evidence for shear in outcrop. Shear could be identified from offset foliation planes or crosscut veins, rhombochasm structures, tension gashes, wingcracks, or slickenlines on the vein face (Figure 2). High pore pressures that have been invoked to explain triggered tremor (e.g. Shelly and Hardebeck, 2006) suggest shear fractures could be accompanied by quartz- or calcite-filled veins that form from hydrothermal fluids (*cf.* Fagereng *et al.*, 2011; Hayman and Lavier, 2014). The presence of fluid is also interpreted from geophysical observations of reflectivity and a high attenuation of P-waves in tremor signals (Wech *et al.*, 2012). The foliation in mylonitic rocks may cause the rock to be mechanically anisotropic, providing a preferred orientation for shear failure (Walsh and Brace, 1964; Kerrich and Allison, 1987) so shear fractures may preferentially form in similar orientations to the foliation. Additionally, low stress drops inferred for LFEs would be represented as small offsets relative to the lengths of shear fractures (Fletcher and McGarr, 2011; Fagereng, 2011). Incremental opening or continued deformation of shear failures could represent successive tremor bursts (Fagereng *et al.*, 2011). As tremor occurs repeatedly at the tremor source, shear structures would be formed coeval with ductile deformation, and be subsequently ductilely deformed (Beroza and Ide, 2011), resulting in cyclical deformation of veins and fractures in the rock record.

## 2.3. Geologic setting

The study area for this work is located north of Tioga Pass, Yosemite National Park, California, at an elevation of ~3000 m. High elevation and recent glaciation have resulted in large areas of exposure. This study focused on a portion of the Steelhead Lake shear zone that is exposed near Saddlebag Lake, within the Saddlebag Lake roof pendant.

### *2.3.1. Tectonic setting and geologic history*

The Sierra Nevada is composed of tectonically accreted Paleozoic and Mesozoic terranes intruded by the large volume Mesozoic intrusive rocks of the Sierra Nevada batholith (Saleeby, 1981). The granitic batholith trends north to northwest and is bound to the east and west by Paleozoic miogeoclinal sedimentary sequences and Paleozoic and Mesozoic eugeosynclinal strata, respectively (Bateman *et al.*, 1962). Paleozoic miogeoclinal sedimentary units were deposited along a passive margin on the western edge of North America and are mainly composed of slate, marble, and schist. (Schweickert and Cowan, 1975; Greene and Schweickert, 1995). The Paleozoic miogeoclinal rocks were faulted, folded, and metamorphosed by the Antler and Sonoma orogenies driven by subduction in the Paleozoic (Schweickert and Lahren, 1987).

Subduction of the Farallon Plate along the western margin of North America in the Mesozoic initiated arc magmatism in the Sierra Nevada. Following the initiation of arc magmatism, Mesozoic volcanic and sedimentary rocks were deposited in the backarc basin (Schweickert and Cowan, 1975). A regionally extensive unconformity defines the boundary between the Paleozoic and Mesozoic strata (Schweickert and Lahren, 1987; Stevens and Greene, 1999). Mesozoic volcanic units include Permian- Triassic andesite and rhyolite packages interpreted to record the presence of a collapsed Triassic caldera in the east-central Sierra

(Schweickert and Lahren, 1999). In the late Jurassic, island arc collision caused the Nevadan orogeny, deforming both the Paleozoic and Mesozoic sequences of rocks (Brook, 1977).

The central Sierra Nevada batholith is composed of four major intrusive suites, including the Tuolumne Intrusive Complex (TIC), which bounds the western edge of our study area (Bateman, 1992). Radiometric dating of the TIC indicates an emplacement age of ~88 Ma (Coleman *et al.*, 2009). Episodic contractional deformation, subsidence, and burial deformed the backarc region in the late Mezoic and early Cenozoic (Dunne and Walker, 2004). The region subsequently experienced uplift and erosion in the Cenozoic (Brook, 1977; Stevens and Greene, 1999). Erosion and glaciation have exposed the country rocks to the Sierra Nevada batholith, consisting of the pre- to syn-intrusion metasedimentary and metavolcanic sequences, in a series of NW-SE trending roof pendants (Brook, 1977; Stevens and Greene, 1999). Roof pendants follow a NW-SE linear trend through the eastern Sierra Nevada, contain similar rock units, and contain series of shear zones that are collectively referred to as the Sierra Crest shear zone system (Greene and Schweickert, 1995). This system includes the Gem Lake shear zone within the Ritter Range roof pendant to the south of our study area and the Cascade Lake shear zone to the north (Cao *et al.*, 2015)

The Saddlebag Lake roof pendant contains metamorphosed Paleozoic to Mesozoic rhyolite, dacite, and andesite as well as conglomerate, sandstone, siltstone, and shale affected by the Steelhead Lake shear zone (Albertz, 2006; Brook, 1977; Schweickert and Lahren, 1987). Within the pendant, the Ordovician Palmetto formation is unconformably overlain by Triassic metavolcanic sequences of rhyolite and andesite, including an andesite package of significant thickness (~1500 m) (Schweickert and Lahren, 1987). Triassic metavolcanic rocks are overlain by Jurassic rocks, informally referred to as the Jurassic Sawmill Canyon Sequence (Schweickert

and Lahren, 2006). The Sawmill Sequence is composed of cross-bedded quartzite, phyllite, and calc-silicate with local limestone, conglomerate, volcaniclastic rocks and schists (Cao *et al.*, 2015). Cretaceous metasedimentary units near the pluton boundary represent only a small section of the shear zone stratigraphy (Paterson *et al.*, 2015).

*2.3.2. Steelhead Lake shear zone*

The Steelhead Lake shear zone-fault system is well developed along the eastern margin of the Tuolumne Intrusive Complex (TIC) (Figure 3). The shear zone has been mapped over about 30 km along strike and trends N-NW (Cao *et al.*, 2015). Structural fabrics within the shear zone deform both the Saddlebag Lake pendant units and TIC indicate that the Steelhead Lake shear zone, in addition to others within the Sierra Crest shear zone system, was actively deforming in the Cretaceous during the intrusion of the TIC (Greene, 1995; Albertz *et al.*, 2005). Ages of intrusive units within the TIC are between ~86-94 Ma, recording up to 8 Ma of magmatic chamber growth and emplacement processes (Paterson *et al.*, 2008). Temperatures within the TIC were between the granodiorite solidus and 760°C, varying both spatially and temporally in the shear zone wall rocks (Paterson *et al.*, 2008). Peak temperatures decreased with time post-intrusion as a function of multiple factors including the initial temperature of the melt and the wall rock, the size of the intrusion, and the duration of magma emplacement (Paterson and Tobisch, 1992). Emplacement temperatures of nearby plutons, including the Green Lake, Soldier Lake, and Cathedral peak plutons, were greater than 700°C (Cao *et al.*, 2015). If the Steelhead Lake shear zone is considered a segment of the Sierra Crest system, the overall length of the structure would be greater than 150 km (Tikoff and Greene, 1997; Cao *et al.*, 2015).

All lithologies within the shear zone show evidence for contact and regional metamorphism (Schweikert and Lahren, 1987). Additionally, all metamorphosed units contain a northwest-trending foliation and isoclinal outcrop-scale folds previously interpreted to relate to the Late Jurassic Nevadan orogeny and possibly also Triassic or Cretaceous deformation events, and are distinct to the Steelhead structures (Brook, 1977; Schweickert et al., 1984; Schweickert and Lahren, 1987; Nokleberg and Kistler, 1980; Tobsch and Fiske, 1982). *Schweickert and Lahren* (1987) attributed a west-north-west-trending crenulation cleavage visible in the Triassic metavolcanic sequence to Cretaceous deformation. Intrusion of the Tuolumne Intrusive Suite (TIC) in the Late Cretaceous resulted in contact metamorphism of country rocks (Kerrick, 1970).

The Steelhead Lake shear zone contains isoclinal folds, transposed bedding and veins that overprint the regional metamorphic structures. A phase of predominantly strike-slip brittle deformation crosscuts the shear zone (Hartman, 2013; Hartman, *in prep*.). Faults cut (and displace) dikes, mylonitic rocks and veins. In some portions of the brittle faults, large (~10 m thick) quartz veins along the fault trace indicate significant volumes of fluids were involved in the late-stage brittle deformation. Epidote-filled fractures that splay from the strike-slip faults and cut the shear zone rocks are abundant.

### 2.4. Field and microstructural observations

Evidence for potential synchronous ductile and brittle deformation and accompanying fluid flow was obtained by mapping veins within the Steelhead Lake shear zone. Key exposures were selected within a 0.5 km wide area extending ~2 km along strike of the shear zone to the west and south of Saddlebag Lake where multiple sets of crosscutting veins were exposed. Vein relationships and characteristics in these exposures were used to infer the chronology of

deformation and conditions under which structures formed. Observations of shear deformation parallel to the foliation were the focus of our study, so exposures containing these structures were selected for detailed mapping (Appendix A). Horizontally rectified photographs of the exposures were generated with the Structure-from-Motion method using Agisoft PhotoscanPro (following Johnson *et al.,* 2014). The rectified images were used as basemaps for annotation in the field. Absolute positions and a physical scale for the images were calculated with a real-time kinematic (RTK) differential GPS (accurate to ± 2 – 3 mm).

*2.4.1. Steelhead Lake Shear zone*

The Steelhead Lake shear zone is defined by the presence of mylonites, re-folded folds, a steeply dipping foliation, and steeply plunging lineations affecting the metamorphic rocks of the Saddlebag Lake pendant. Fold vergence, S-C structures in mylonites, asymmetric clasts in volcanic rocks, and delta structures that are prevalent at the millimeter-scale all indicate dextral shear in sub-horizontal exposures. Asymmetric clasts in sub-vertical exposures indicate west side-up normal shear. The foliation is defined by preferred orientations of chlorite and muscovite grains and compositional banding at the millimeter- scale to the meter- scale. Flattening is demonstrated by isoclinal and transposed bedding and in folded veins with axial surfaces parallel to the foliation of the rock. Foliation attitudes are mostly consistent throughout the shear zone, ranging in strike from 294 to 358° and dip from 46 to 88° (Figure 4). A penetrative mineral lineation defined by aligned elongate grains and grain aggregates of chlorite, quartz and/or diopside, depending on the rock type, is moderately to steeply plunging on average 55° to the southeast. The combination of steep lineations, evidence for both flattening approximately normal to the shear zone and dextral shear parallel to the shear zone, indicates the deformation

was dextral transpression. Similar features have been recognized in nearby shear zones (Tikoff and Greene, 1997).

Mylonitic rocks are only present within ~350 m of the pluton boundary and are defined by a well-developed S-C fabric within a fine-grained groundmass. The groundmass contains rotated feldspar porphyroclasts and compositional layers, which define the foliation of the rock. Layers are composed of quartz and chlorite with minor biotite and epidote, alternating every 1 mm and bending around small (0.5 mm) feldspar porphyroclasts. Units between 350 m and 1.5 km from the pluton boundary include ductile deformation structures such as folds, foliations, and the mineral lineation. These structures are absent in units farther than 600 m from the pluton.

All Mesozoic rocks within the shear zone are fine-grained and are composed predominantly of quartz (Figure 5). The Triassic andesite (Figure 5C, 5D) and rhyolite (5E) units are very fine-grained (average grain size <0.05 mm), and are composed of quartz, plagioclase, chlorite, and muscovite. The andesite is accompanied by minor rutile and hornblende. Chlorite in metavolcanic units sometimes occurs in small clusters of grains along quartz grain boundaries, appearing as a web across the host rock. Otherwise, epidote grains are euhedral within the groundmass. Most plagioclase phenocrysts have been replaced by sericite. Quartz phenocrysts exhibit undulose extinction and irregular grain shapes caused by dynamic recrystallization. Foliation of the andesite units is defined by the preferred orientation of spaced, elongate muscovite and chlorite grains. Discrete bands of fine-grained sericitized feldspar grains define the foliation of the rhyolite unit. Crenulation cleavage is visible in some muscovite and chlorite-rich samples from near the pluton boundary. These mica- rich samples may represent ashy interlayers within the andesite when it was deposited.

The Jurassic metasedimentary rocks are most commonly adjacent to the TIC margin in our study area (Figure 3), and contain abundant veins. Consequently, the majority of the observations of veins in mylonitic rocks come from these units. The Jurassic unit can be divided into silicate (Figure 5A) and calc-silicate (Figure 5B) sub-units, which are interlayered every ~10 m. The former is largely homogeneous, with minor compositional variations occurring at a few-cm scale. The silicate sub-unit contains a fine-grained (~0.3-0.5 mm), equigranular groundmass of quartz and plagioclase. Epidote occurs as an accessory mineral scattered throughout the groundmass. Tabular euhedral muscovite and chlorite grains are interspersed throughout the silicate sub-unit and are aligned parallel to the compositional banding, defining the foliation. Variations in the chlorite and muscovite content within the rock define the minor compositional changes within this sub-unit.

The more calcium-rich Jurassic sub-unit has a similar mineral assemblage to that of the silicate sub-unit, with the addition of diopside and epidote. The calcium-rich sub-unit has a foliation defined by strong compositional banding at both millimeter- and meter- scales. Banding at a 5-50 mm-scale is representative of transposed and isoclinal bedding in the rock unit. At the grain- scale, bands are 1-2 mm thick and are composed of quartz and chlorite. The grains are asymmetric to the foliation in the direction of the shear zone boundary, defining the S-C fabric of the rock.

The deformation is different in the two Jurassic subunits (Figure 6). Veins within the silicate-rich subunit are linear and are weakly to moderately boudinaged (Figure 6A, 6B). These veins are thin (2-4 mm) and are common throughout the outcrop. Veins in the calc-silicate subunit are strongly boudinaged and extensively folded, commonly with refolded folds (Figure 6C). Veins in this subunit are much less common than in the silicate-rich unit.

*2.4.2 Veins*

*2.4.2.1. Field data*

Quartz, tourmaline, and epidote veins are common within all Mesozoic units cut by the Steelhead Lake shear zone. Quartz veins range in thickness from 1-5 mm and are formed in two predominant sets, one cutting the foliation and one parallel to sub-parallel to the shear zone foliation. Veins parallel to the foliation are straight and continuous or folded with the foliation and are boudinaged in vertical and horizontal exposures. Veins cutting the foliation are heavily folded (transposed) and are not boudinaged. Tourmaline veins invariably cut the foliation and are commonly tightly folded. They range in thickness from 1-20 mm, and most are surrounded by a halo of lighter colored rock. Some larger tourmaline veins include interior aligned quartz lenses at their centers that have folded with the vein (Appendix C). Leucogranite dikes are also found throughout the area and cut the foliation of the rock. Dikes range in thickness from a few millimeter to several meters, and many are folded. Multiple sets of epidote veins are present. One set is present within recrystallized quartz veins along grain boundaries. Numerous epidote veins that cut all other vein compositions branch from the brittle faults, and are interpreted to have formed late in the deformation history of the system.

Some quartz veins sub-parallel to the foliation crosscut other structures and show measurable shear offsets. The evidence for shear is consistent with the structures defined in Figure 2, but the most common structural indicators include rhombochasm structures (Figure 7A) and offset veins (Figure 7B). There is an average 5° local misorientation between the foliation and vein orientations. Foliation sub-parallel veins have a quartz fill and an average thickness of 2-4 mm. Quartz in these veins is generally coarse-grained and transparent to white. The foliation sub-parallel veins are tightly spaced in outcrop, commonly separated by less than 1

m perpendicular to vein strike, and in some areas, they are spaced every ~10 mm (Figure 6A, 6C). All of the veins in the foliation sub-parallel set are locally parallel but non-coplanar so do not connect. Lengths and displacements of 45 veins were measured. The lengths of these veins range from 0.4 to 4.8 m, though many of the lengths are minimum estimates because the veins extended beyond the length of an exposure. Apparent dextral shear offsets along foliation-parallel veins ranged from 2 to 30 mm, with an average apparent offset of 12 mm. Foliation sub-parallel veins are commonly boudinaged in horizontal and vertical exposures and fold with the foliation of the host rock where the foliation is folded. Boudins in horizontal exposures are typically asymmetrical and deformed by necking into depressions and swells parallel to the foliation. Both isolated fragments and pinch-and-swell structures in foliation sub-parallel quartz veins record thinning and extension.

Commonly, the foliation sub-parallel veins are the only type of vein in an exposure. However, where veins at larger angles to the foliation are present, the foliation sub-parallel veins both offset the high angle veins and are crosscut by them (Figure 8). Quartz and tourmaline veins cutting the foliation are gently- to isoclinally-folded. Folded quartz and tourmaline veins commonly have axial surfaces parallel to the foliation. Veins of all compositions that occur at an angle to the foliation are planar and cross-cut all other folded veins.

*2.4.2.2. Microstructural data*

Thin sections of each sample were prepared perpendicular to the lineation and orthogonal to the foliation containing the lineation from samples of foliation sub-parallel veins 320-650 m from the pluton boundary. Microstructures of foliation-parallel veins fall into four distinct groups (Figure 9). Some samples show intermediate textures representative of two groups. Quartz

textures, grain shapes, and various dynamic recrystallization mechanisms define these groups as follows:

(1) Quartz grains are subhedral and elongate (grain sizes ranges from 0.05 mm to several millimeters) with grains exhibiting undulose or patchy extinction (Figure 9A). The alignments of the long axes of all grains are at 40° angle to the overall orientation of the vein. Small, rounded grains line the edges of larger grains in a core-and-mantle structure (Gifkins, 1976). This group shows characteristics similar to Regime 1 of *Hirth and Tullis* (1992), also referred to as bulging recrystallization (BLG) (Passchier and Trouw, 2005).

(2) Quartz grains are elongate and equigranular, with small, slightly elliptical recrystallized subgrains (average grain size ~0.05 mm) grouped in clusters (Figure 9C). All grains are aligned in a preferred orientation at a slight (~20°) angle to the orientation of the vein edges. Quartz grains exhibit a hybrid interlobate- amoeboid texture. Undulose extinction is visible in larger grains, which have more elliptical shapes with aligned long axes. These characteristics are consistent with subgrain rotation recrystallization (SGR), or Regime 2 of *Hirth and Tullis* (1992) (Passchier and Trouw, 2005).

(3) Quartz grains (~2 mm in diameter) are equigranular with interlobate grain boundaries (Figure 9E). Few to no subgrains are present, and extinction is uniform within the grains. The grains in this group are representative of grain boundary migration (GBM) recrystallization, or Regime 3 of *Hirth and Tullis* (1992) (Passchier and Trouw, 2005).

(4) Grains are euhedral, equigranular (grain size 0.5-0.8 mm) and polygonal (Figure 9F). Triple-junctions are prevalent, and extinction is uniform throughout individual grains. These characteristics are representative of static recrystallization (Passchier and Trouw, 2005).

Two intermediate textures have also been defined. These samples include evidence of deformation consistent with a combination of BLG/SGR and SGR/GBM recrystallization. The former includes prevalent recrystallized grains, but the additional presence of a core- and- mantle texture (Figure 9B) and the latter contains both elongated recrystallized grains with an interlobate-amoeboid texture (Figure 9D). There is no direct correlation between the microtexture of the quartz vein and distance from the pluton.

Quartz crystals within foliation-parallel veins contain fluid inclusions ranging from 5 to 15 μm in diameter. Petrographic analysis was performed on fluid inclusions in four samples to determine their composition. The liquid phase of the inclusions appear bright in thin section, whereas the gas phase, appears darker. No clathrate is present in the inclusions. Further, no freezing of gas bubbles or evidence of $CO_2$ was observed, indicating that the fluid inclusions are a binary aqueous electrolyte system containing $H_2O$-NaCl and that the gas bubbles contain water vapor.

Multiple sets of fluid inclusion planes are present. Samples for fluid inclusion analysis from foliation-parallel quartz veins were taken from various locations throughout the shear zone. These samples are from all four microstructural groups. Each quartz sample analyzed contains at least one set of fluid inclusion planes, and 3 of the 4 samples contain two independent sets. Set 1 is curviplanar, running parallel to sub-parallel to the orientation of the quartz vein and extending across several grains. This set has fluid inclusions scattered irregularly throughout the extent of the planes. Less than 10 planes of Set 1 were observed across the entire quartz vein in each sample. Set 2 contains linear planes of fluid inclusions, at an angle of 80° in the plane of the section (cut perpendicular to the foliation and parallel to the lineation) to the Set 1 and terminating at grain boundaries. These planes are irregularly spaced throughout the vein.

Inclusions are evenly distributed within each plane. Following the classification methods of *Roedder* (1984), both sets formed as secondary inclusions, defined as inclusions trapped during post-crystallization fracturing.

Fluid inclusion analysis was performed using a Linkam 600 heating-freezing stage attached to an Olympus BX50 petrographic microscope. Homogenization temperatures (Th), first ice melt ($T_{eutectic}$), and final ice melt ($Tm_{ice}$) temperatures were measured (Appendix B) following the method of *Roedder* (1984).

Homogenization temperatures are different for Set 1 and Set 2. Average $Th_{total}$ of Set 1 and Set 2 are 360°C ± 24° (1σ, n = 38) and 249°C ± 16° (1σ, n = 60), respectively (Figure 10). Freezing point depressions were very similar between Set 1 and Set 2. For Set 1, average $T_{eutectic}$ is -24.32°C ± 1.2° (1σ, n = 6), and average $Tm_{ice}$ is -1.23°C ± 0.3° (1σ, n = 6). These data indicate salinity of Set 1 of 3.6 wt% (min=3.1 wt%, max=4.2 wt%). Observations of Set 2 indicate the average $T_{eutectic}$ is -24.82°C ± 1.2° (1σ, n = 8), and average $Tm_{ice}$ is -1.47°C ± 0.3° (1σ, n = 6). These data indicate salinity of 2.6 wt% (min=1.9 wt%, max=3.2 wt%). Salinity calculations assume an isochoric inclusion to which nothing has been added post-entrapment (Roedder, 1984).

The pressure of crystallization in plutons adjacent to the Saddlebag roof pendant was between 1 - 2 kbar (Ague and Brimhall, 1988). Because pluton emplacement and shear zone deformation were occurring at the same time, we used these pressures, the calculated salinities, and observed homogenization temperatures to determine a trapping temperature for each set of fluid inclusions. Average trapping temperatures were between 515-680°C for Set 1, and between 320-400°C for Set 2.

The deformation of Set 1 evident in the curviplanar nature of the plane may have deformed the fluid inclusions. If deformation of the fluid inclusions occurred, it is possible these inclusions were re-equilibrated (i.e., changed volume, or lost/gained components). Laboratory experiments have shown that host mineral strength, fluid composition, and inclusion size and shape determine the ease of fluid inclusion reequilibration (Bodnar, 2003). The hardness of quartz requires pressures greater than 2.0 kbar to initiate reequilibration for fluid inclusions 1-15 μm in size (Bodnar *et al.*, 1989). In addition, samples containing $H_2O$-NaCl, like those included in this study, require pressures of ~3 kbar to initiate the reequilibration process (Hall and Wheeler, 1992). There are no fractures of host mineral locally surrounding the fluid inclusions, and the edges of inclusions themselves are not irregular. These observations support that these inclusions have not been reequilibrated. A wider range in homogenization temperatures is often a sign of reequilibration. The range of homogenization temperatures in our data for both sets of inclusions is larger than expected for one fluid inclusion assemblage. However, the reproducibility of homogenization temperatures, which were tested on multiple samples to ensure correct measurement, further signifies that these samples have not reequilibrated (Bondar, 2003). Because of this, observed $T_h$ measurements are interpreted accurately represent homogenization temperatures of fluid.

*2.4.3 Electron backscatter diffraction*

To gain insight into grain size distribution, deformation temperatures, strain, and a constraint on differential stress, electron backscatter diffraction (EBSD) was performed on two samples of foliation-parallel quartz veins exhibiting evidence of SGR recrystallization in the Jurassic metasedimentary rock. This analysis was conducted on a JEOL 6500F Field Emission SEM with an EDS detector at Colorado State University. The data were processed using EDAX

OIM software. Seven to ten areas of the 2 quartz veins (4a, 16a) were analyzed with a 5 μm step-size to map an area of 500 x 500 μm. From these preliminary maps, similar sized areas containing smaller recrystallized grains were selected and scanned again at a 2 μm step size. High-resolution maps were created (Figure 11A), and the data were 'cleaned' by removing areas of pixel clusters that were mis-indexed by the software. To do this, we defined a high-angle subgrain boundary as misoriented by 10° and a minimum grain size as 5 μm. Crystallographic preferred orientation (CPO) patterns were collected and plotted as intensity pole figures for both c- and a- axes (Figure 11B). Pole figures of c-axes are clustered or bimodal with maxima near the center of the plots. These clusters form single girdles and maintain a similar orientation within each individual vein. These bullseye patterns are characteristic of medium T deformation (Passchier and Trouw, 2005). Distributions of a-axes vary across each sample, and are less consistent in sample 16A. The samples maintain a similar pattern across multiple individual scans, specifically in sample 4A. Orientation patterns of a-axes are consistent with observations of CPO patterns of laboratory-deformed quartz showing SGR recrystallization in *Stipp et al.* (2002), indicating dominant prism a slip, and reflecting a medium deformation temperature (Passchier and Trouw, 2005).

Using paleopiezometry, which is based on empirically derived relationships between the grain size of dynamically recrystallized material and stress, we estimated flow stresses for our samples (Handy and Zingg, 1991; Hirth and Tullis, 1992; Stipp and Tullis, 2003). The OIM software calculated average grain sizes and area fractions for the high-quality scans, producing a grain size distribution histogram for each individual scan, both taken from sample 16A. The average grain size for Scan 17 is 17.27 ± 14.87 μm (1σ, n= 404), and the average grain size for Scan 19 is 19.15 ± 12.66 μm (1σ, n = 535). The *Stipp and Tullis* (2003) piezometer was used to

constrain a flow stress for these values. An average recrystallized grain size of 19.15 μm corresponds to a flow stress of ~60 MPa, and an average grain size of 17.27 μm is consistent with flow stresses of ~ 87 MPa.

### 2.5. Stable Isotope Geochemistry

Quartz and tourmaline samples taken from one of the key exposures (Figure 8) were prepared for isotope analysis with the intention of establishing fluid sources of multiple sets of veins. Samples included three quartz and two tourmaline samples from four distinct sets of veins. In the sampled exposure, a large, tightly folded tourmaline vein cuts the foliation; this vein is surrounded by an alteration halo and has inclusions of quartz lenses in the center of the vein (Appendix C). Small fractures in the fold hinges of the tourmaline vein, orthogonal to the vein edge, are filled with quartz. This tourmaline vein is cut by a set of thin (~2 mm), folded quartz veins, which is apparently dextrally offset 36 mm by a 1 mm- thick foliation-parallel quartz vein. The larger tourmaline vein terminates ~10 mm away from the trace of the foliation-parallel quartz vein. A 1 mm wide folded tourmaline vein cuts the quartz-filled shear fracture. All veins in the outcrop are crosscut by thin, non-mineralized fractures in a variety of orientations.

Samples of the veins described above were crushed and sieved at 200-250 microns. A magnetic separator with 10° side tilt, 5° forward tilt, and a magnetic setting of 0.7 A was used to accelerate the separation of tourmaline and quartz grains.

Oxygen and hydrogen isotopic compositions were measured on the ThermoFinnigan DeltaPluxCP light isotope mass spectrometer at California State University Long Beach IIRMES lab (Table 1). Two to four mg of each sample were loaded into the system. These samples underwent laser ablation in the presence of bromine pentafluoride, following the method of Sharp (1990). The resulting $O_2$ gas was converted to $CO_2$ and analyzed by conventional isotope

ratio mass spectrometry. Hydrogen isotopic values were determined using the TC/EA method (Sharp *et al.*, 2001) that utilizes the flash reduction of $H_2O$ liberated from mineral samples at 1450°C to produce $H_2$ gas for mass spectrometry. Precision of hydrogen (±2‰) and oxygen (±0.2‰) runs was determined using the NBS-30 biotite (δD = –65.7; Gonfiantini, 1984) and Caltech Rose Quartz ($\delta^{18}O$ = +8.45; Taylor and Epstein, 1962) standards.

$\delta^{18}O$ and δD values from the two tourmaline (KC4, KC5) samples (+7.9, –92.6 and +8.0, –95.5) indicate a magmatic fluid source. The proximity of this outcrop to the Tuolumne Intrusive Complex (~390 m) explains these values, and tourmaline is present in dikes related to the TIC. All of the $\delta^{18}O$ values of quartz samples (KC1, KC2, and KC3) (+2.5 to +7.2) are lower than the tourmaline values, suggesting a meteoric or mixed-fluid source (Figure 12). The youngest vein yielded significant amounts of both quartz (sample KC3) and tourmaline (sample KC4), but the $\delta^{18}O$ values were significantly different for the two mineral phases from this sample.

Water $\delta^{18}O$ values (quartz = –0.9 to +3.8, tourmaline = +7.0) were calculated using oxygen isotope fractionation factors for quartz-water (Matsuhisa *et al.*, 1979) and tourmaline-water (Zheng, 1993) for a temperature of 350°C. This temperature is consistent with the metamorphic assemblage and dynamic recrystallization mechanism in the quartz vein at this outcrop. Published water $\delta^{18}O$ values for the Tuolumne Intrusive Complex (TIC) range from +7.7 to +10.0% (Kistler *et al*., 1986, Lackey *et al*., 2008). Regionally, quartz $\delta^{18}O$ values from Central Sierran intrusive rocks range from +8.8 to +12% (Lackey *et al.*, 2008), so our lower quartz $\delta^{18}O$ values document the involvement of a non-magmatic fluid (most likely meteoric-hydrothermal) in the Steelhead Lake shear zone.

## 2.6 Interpretation

The Steelhead Lake shear zone deformed as a result of flattening and dextral shear at elevated temperatures, with increased temperatures occurring as a result of intrusion of the TIC. Deformation of dikes emanating from the TIC indicates the shear zone was actively deformation during intrusion. Magmatic foliations within the TIC also indicate deformation following the intrusion of the pluton (Žak and Paterson, 2005). In this section, we review the field, microstructural and isotopic data to establish the temperature and fluid conditions during the mixed rheology deformation.

Three sets of data constrain the temperature of the ductile deformation in the Steelhead Lake shear zone: the host rock mineral assemblage, the dynamic recrystallization mechanisms identified in quartz, and the trapping temperatures of the quartz vein fluid inclusions. Aligned chlorite and muscovite grains define the foliation in most of the rock units in the shear zone, reflecting deformation at low- to mid-greenschist conditions. In some cases, the platy cleavage of the chlorite grains indicates it is a retrograde pseudomorph after biotite (Figure 5F). The presence of biotite suggests possible upper-greenschist facies conditions and temperatures above 400°C. The lack of amphiboles and garnet-group minerals or their retrograde pseudomorphs indicates prograde metamorphism reached its peak at the biotite zone of the greenschist facies.

The deformation of the host rock and dynamic recrystallization mechanisms visible in foliation-parallel quartz veins record deformation at a range of temperatures. The presence of all three dynamic recrystallization mechanisms in quartz veins indicates a temperature range of 300-500°C over the duration of deformation. Bulging recrystallization occurs in ductile conditions under temperatures of 300-400°C, subgrain rotation recrystallization is associated with temperatures of 400-500°C, and grain boundary migration recrystallization is consistent with

temperatures of 500-700°C (Stipp *et al.*, 2002). In addition to temperature, rates of recovery are also affected by strain rate and the presence of water. A decrease in the strain rate increases the rate of dislocation climb across grain aggregates, and the addition of even just trace amounts of water decreases the deformation temperature ~100°C (Hirth and Tullis, 1992). Based on these experimentally derived data, we conservatively suggest recrystallization textures reflect temperatures greater than 400°C.

An overall retrograde thermal history is reflected in two distinct sets of fluid inclusions planes visible in the foliation-parallel quartz veins. Planes of Set 1 were trapped at ~515-680℃. These planes are slightly folded and unaffected by grain boundaries, suggesting they most likely formed soon after ductile deformation and recrystallization. Set 2 fluid inclusion planes are planar, as observed in thin section. Thermobarometry indicates these planes were trapped at a temperature of ~320-400℃. Additionally, the terminations of Set 2 planes at grain boundaries suggest an episode of fracturing and fluid assisted cementation post- ductile deformation, indicating they formed later in the deformation history than Set 1. These planes may also have formed under diagenetic conditions within clasts or individual grains. Set 1 fluid inclusion planes reflect higher trapping temperatures whereas more planar fluid inclusion sets indicate lower trapping temperatures; this evidence is most consistent with a retrogressive temperature path.

Though high (~550-650°C) temperatures in the aureole of the TIC have previously been reported, a spatial variability of temperatures is observed (Kerrich, 1970). Peak temperatures related to the intrusion decrease with increasing distance from the pluton boundary. Spatial and temporal distributions of temperature during- and post-intrusion may be reflected in various deformation structures and dynamic recrystallization mechanisms across the shear zone. Structures recording deformation at higher temperatures include the foliation, S-C fabrics in

mylonites, crenulation cleavages, steep lineations, meter-scale folds, and grain boundary migration recrsytallization. Additionally, fluid inclusion trapping temperatures and evidence for dynamic recrystallization reflect deformation at temperatures consistent with the intrusion of the TIC. Formation of veins at discrete times and in varying locations during the cooling of the rock post-intrusion record a range of temperatures.

Veins present throughout the shear zone record the movement of fluids throughout the deformation history. The various mineral fill of veins - quartz, tourmaline, and epidote, and batholith-related granitic dikes - indicates multiple pulses of fluid intrusion. Additionally, there are numerous veins of all types, in particular quartz veins, both showing a repeated fracturing and suggesting multiple episodes of fluid influx within the shear zone. Vein sets are found in multiple orientations, having formed both parallel to and across the foliation of the rock. Later-formed epidote veins, interpreted to be related to late-stage brittle faulting, indicate vein formation during both ductile and brittle phases of shear zone deformation. The crosscutting relationships of the veins indicate multiple episodes of vein formation over time, representing fracturing events over shear zone deformation.

Complex crosscutting relationships of veins at the outcrop scale indicate synchronous brittle and ductile deformation. Vein formation occurred by brittle fracture and subsequent mineralization. Many veins are folded, sheared, and/or boudinaged, showing the brittle structures subsequently underwent ductile deformation. However, the field relationships show that brittle-ductile deformation occurred cyclically. For example, in Figure 8, the quartz-filled shear fracture, defined by dextral offset of a folded older vein, is cut by younger quartz and tourmaline veins. These younger veins cut the foliation at an angle and are folded.

Shear offsets are present on some foliation sub-parallel quartz veins. The apertures of these veins are all of the order of millimeters, and all are filled with quartz. These characteristics suggest a component of opening in addition to shear during vein formation. Because cataclastic deformation, typically expected to form as a result of brittle shear failure, is not present along vein boundaries at a millimeter-scale, these fractures may have formed as formed by fluid-assisted mixed-mode fractures. Boudinage of many of the foliation sub-parallel quartz veins with asymmetrical boudin necks serves as evidence that they experienced flattening and shear following formation. In addition, the boudins indicate the quartz in the veins was more competent than the surrounding rock at the time of boudinage. The dynamic recrystallization mechanisms and fluid inclusion data mentioned above are taken from these veins, constraining the vein formation to have occurred between 300 and 680°C.

Stable isotope measurements support the presence of either two sources of fluid or segregated migration paths that resulted in increased fluid-rock interaction as a result of longer fluid residence times in the rock. In particular, the disequilibrium in the $\delta^{18}O$ values of KC3 (quartz) and KC4 (tourmaline), which originated from the same vein, suggests a complex fluid history. There are two possible explanations for this disequilibrium. The first is that the discrepancy between the $\delta^{18}O$ values in these samples records the isotopic signature of two independent fluid sources within the vein. Quartz lenses were observed in thin section in the middle of the large tourmaline vein of sample KC5 (Appendix C). These lenses are folded with the tourmaline vein showing that they formed prior to folding but after the tourmaline had precipitated from the original magmatic fluid. Based on field observations, it is likely that the quartz lens inclusions within the larger, older tourmaline vein are most likely also present within the smaller, younger tourmaline, though at a much smaller scale. I suggest quartz lenses may be

representative of a second, much later pulse of meteoric fluid. Fluid inclusion data reflecting salinities of 2.6 wt% and 3.4 wt% for secondary fluid inclusion planes support a meteoric origin of the second pulse of fluid. The presence of meteoric fluids indicates the shear zone deformation was not entirely driven by the presence of the nearby TIC, and that the deformation here is not unique to systems near magmatic intrusions. The second possible explanation for this isotopic disequilibrium is late-stage fluid-rock interaction. I infer that tourmaline veins originated from a magmatic source at various stages in the deformation history, most likely the Tuolumne Intrusive Complex. Though quartz and tourmaline are resistant to isotopic exchange, the infiltration of later fluids through re-opened fractures may have altered the isotopic values of the quartz but not the tourmaline (LeRouge and Bouchot, 2009).

Another complication to the isotopic data is the range in $\delta^{18}O$ values of the three quartz samples. This heterogeneity likely results from varying degrees of fluid-rock interaction between the fluids that migrated through the Steelhead Lake shear zone and precipitated quartz and tourmaline in the sets of fractures described above and the country rock (Zheng *et al*., 1999). Various aspects of fracture formation (timing, orientation, size, connectivity etc.) determine the nature of fluid flow, controlling the amount of interaction between the infiltrating fluid and the wall rock. The $\delta^{18}O$ values from the quartz samples indicate meteoric water at one time infiltrated the shear zone. Isotopic exchange between the infiltrating meteoric fluid and the wall rock results in lower $\delta^{18}O$ values.

In summary, the stable isotope data are most consistent with either the presence of two distinct fluids (magmatic and meteoric) or evidence for extended fluid-rock interaction. High fluid pressures are marked by the episodic intrusion of magmatic fluids (tourmaline veins described here, and also dikes), which is recorded by both the oldest and youngest veins within

the chronology of the sample set shown in Figure 8. However, infiltration of meteoric water is consistent with sub-lithostatic pressures. I suggest the high fluid pressures indicated by these data may have driven the system to failure. Mode I fractures forming across the foliation of the rock may represent hydrofractures, indicating the pore fluid pressure was greater than $\sigma_3$ during failure. There is no evidence suggesting pore pressure approached lithostatic pressure.

Temperatures decreased to ~380℃ and lower over the course of shear zone deformation, culminating in a brittle fault system (Hartman, *in prep.*). Within the ductile phase, veins that were subsequently folded and boudinaged record cyclical discrete fracture events followed by ductile deformation and therefore mixed rheology deformation. Fluids were present within the shear zone at all stages of deformation, and are recorded by quartz and tourmaline veins as well as fluid inclusion planes. Isotopic evidence suggests two independent sources of fluids infiltrated the shear zone. Fluid inclusion data indicates distinct trapping temperatures of two sets of fluid inclusions with similar salinities.

**2.7 Discussion**

This research focuses on observed brittle-viscous deformation in a transpressive shear zone in the Sierra Nevada. Cyclical brittle and ductile deformation of veins in shear zones has been studied previously in other areas. Based on vein orientations, previous research interpreted veins to form by the infilling of extension (mode I) fractures, and that vein orientations were the result of large stress rotations (Kerrich and Allison, 1978; Fisher *et al.*, 1985; Hodgson, 1987; Henderson and McCaig, 1996; Nguyen *et al.*, 1998). In contrast to previous work, I recognized evidence for shear offset across the foliation sub-parallel veins in the Steelhead Lake shear zone. This kinematic information suggests that shear fractures parallel to the foliation, which formed

an anisotropic surface preferential to failure (Shea and Kronenberg, 1993) are consistent with the same stress field as the mode I fractures that form across the foliation (Figure 13). A major re-orientation of the stress field is not required for the formation of mode II cracks along the foliation of the rock. Assuming the flow stress recorded by the dynamically recrystallized quartz grains is a proxy for the differential stress in the system, I propose that the mechanical anisotropy of the foliated shear zone rocks promotes shear failure close to parallel to the foliation at high differential stress. This may be recorded by the average recrystallized grain sizes calculated with EBSD and their related flow stresses, which indicate veins deformed under high flow stresses (~60- 87 MPa). The tensile strength, T, strength of similar rocks to those in this study is typically 10 MPa (Etheridge, 1983). Large flow stresses are consistent with the conditions for shear fracture, i.e. $(\sigma_1-\sigma_3)/2 > 2T$. I suggest tensile failure formed across the foliation as a result of low differential stress and increased fluid pressure. Strain hardening during deformation increased the differential stress in the system, promoting shear failure parallel to the foliation. Following failure, stress relaxation and deformation of the veins occurred, forming the cyclical brittle and ductile deformation visible in outcrop.

The observed vein sets record brittle failure within a viscous shear zone, but the cause of the mixed rheology is less clear. Previous research (Hobbs *et al.*, 1986; Hayman and Lavier, 2014; Fagereng, 2014) has proposed two general models for the mechanism that causes nucleation of brittle failure within a viscous shear zone resulting from perturbations during steady state creep deformation.

Hobbs *et al.* (1986) proposed that ductile instabilities form as a result of transient strain hardening followed by stress relaxation. They suggested that increased temperature due to extra dissipation of heat as a result of strain hardening in response to an external strain or strain rate

perturbation causes thermal-weakening, resulting in instability. This model requires the relaxation rate to exceed the stiffness of the system for instability (and fracture) to occur. In their work, Hobbs *et al.* (1986) related ductile instabilities to the formation of pseudotachylytes in the ductile regime. However, Hobbs *et al*. (1986) note that the presence of fluids or low mean stress could cause instabilities to result in cataclasites or veins. The Hobbs *et al.* (1986) model also emphasizes the importance of strain or strain rate perturbations to the nucleation of brittle fractures in a ductile regime. Factors such as teleseismic waves, mechanical heterogeneity, earth tides, fluctuations in pore pressure, or fluctuations in loading rate are often associated with triggered tectonic tremor, suggesting a connection between the Hobbs *et al.* (1986) model and tremor because the model requires a strain perturbation to nucleate instability.

The second model, proposed by Hayman and Lavier (2014), suggests mixed-mode fluid-filled fractures form as a result of coupled fracture and viscous flow in a shear zone containing heterogeneous material. This model requires both a rheological contrast between media within the shear zone and an elevated fluid pressure. Hayman and Lavier (2014) based their model on observations of fractures within meter-scale relatively strong lenses inside a shear zone that deformed via viscous deformation. They inferred that fracture occurred due to long-term storing of elastic strain, and proposed an analytical model for the occurrence of slow-slip events, defined as episodic strain transients and accompanied by tremor, at depths consistent with viscous deformation. Field observations that indicate mixed-rheology systems were also presented by Fagereng *et al.* (2014). Fagereng *et al.* (2014) present a model that requires a system containing both strong and weak material in which elevated strain rates are accommodated viscously by one material and by brittle failure in the other. Resulting shear fractures in rigid mafic lenses are representative of tectonic tremor in the geologic record.

The deformation observed in the Steelhead Lake shear zone shows consistencies with both of the above models. The Hayman and Lavier (2014) study suggests tremors are represented in the geologic record as quartz-filled veins in a system that deformed under a mixed-rheology. Field observations indicate quartz veins formed within both Jurassic subunits, however veins formed at a higher density within the more competent Jurassic subunit. Veins in the calc-silicate unit are heavily folded and rotated with the foliation (visible in the banding of the rock), while veins in the silicate-rich member are linear, longer and continuous across the outcrop. These veins only fold slightly when the foliation is folded. The calc-silicate metasedimentary rocks therefore show evidence for greater non-coaxial strain than the silicate-rich member. The difference in deformation between the two Jurassic metasedimentary sub-units is interpreted to be representative of a rheological difference between the two. The presence of two different rheological units is consistent with the mechanical interpretation of the Hayman and Lavier (2014) and Fagereng (2014). Evidence of a high vein density in the Jurassic silicate subunit suggests the Hayman and Lavier (2014) model could explain the cause of this deformation. Further, the presence of episodically formed quartz veins indicates a locally high pore pressure, another criteria of the latter model. Strain accumulation within the more rigid silicate units could nucleate fractures within more rigid units, a sequence of events attributed to the Hobbs *et al.* (1986) model for ductile instabilities.

There are, however, a few inconsistencies that need to be addressed. First, the structures that result from failure, or ‘ductile instabilities’, in our study are quartz veins as opposed to the frictional melt studied by Hobbs *et al.* (1986) Relatively low effective normal stresses may have been prevalent due to the presence of fluid in the Steelhead Lake shear zone system, suggesting a lower rate of frictional heating. Under these conditions, fractures will form instead of

pseudotachylyte. It is also possible that the fractures in our study may have formed as mixed-mode fractures, considering no cataclastic material is preserved surrounding the fractures. Second, the presence of brittle structures in the calc-silicate unit indicates the rheology contrast between the Jurassic sub-units is not identical to the units in the Hayman and Lavier (2014) model.

The strain hardening stage of deformation present in the interpretation of vein formation in this study (Figure 13) is also present in both previously published mechanical models. Strain hardening could reflect either a strain perturbation to the system (Hobbs *et al.*, 1986) or an accumulation of stress in the more competent unit (Hayman and Lavier, 2014). Both mechanisms promote the increase of differential stress and subsequent nucleation of brittle fractures in a ductilely deforming system.

*2.7.1 Do these veins represent tremor?*

One goal of this study was to assess whether there is a correlation between the structures present in the Steelhead Lake shear zone and seismic tremor. I have not identified definitive evidence of seismic slip (such as pseudotachylytes; Sibson, 1975), in the shear zone, but some of the characteristics of the deformation are consistent with a tremor source. As previously discussed, temperatures reflected in the microstructures of quartz in the veins indicate deformation temperatures of 300 - 500°C. These temperatures are consistent with the depths of seismic tremor, observed to be 20-30 km on transform faults, at inferred temperatures of 500-1000°C (Thomas *et al.*, 2009; Shelly and Hardebeck, 2010; Wech *et al.*, 2012). The attenuation of P- waves in tremor signals paired with a high reflectively reflect high pore pressures indicate fluid presence near tremor locations. As a result, high fluid pressures are interpreted as a condition under which tremor occurs (Wech *et al.*, 2012). I infer that the quartz veins in this

shear zone are a product of high pore pressures during the time of shear zone deformation. The multiple pulses of fluid (magmatic and meteoric) indicated by the stable isotopes reflect a continued presence of fluid in the shear zone. Fluid inclusion thermobarometry data suggest fluctuation in temperature over time. The independent P and S body wave arrival times of the LFE signals embedded in the seismic signal of tremor indicate it forms as a shear failure. Further, the cyclical brittle and ductile deformation of the veins is consistent with the repeatable nature of tectonic tremors. VLFEs have moment magnitudes of 3.1 to 3.5 (Ito and Obara, 2007), and would be consistent with millimeter-offset along veins with lengths greater than 100 meters (Wells and Coopersmith, 1994).

However, some aspects of the foliation sub-parallel shear fractures are not comparable to known characteristics of tremor. The depth at which the Steelhead Lake shear zone formed is not consistent with depths or the tectonic setting of seismic tremor. This is estimated to be ~7-9 km based on the observation that the TIC was affected by the shear zone (Žak and Paterson, 2005). Given that the Steelhead Lake shear zone was an intra-arc shear zone, it is not a direct analog for tectonic settings of tremor such as the base of the San Andreas Fault. However, it could be analogous to the tectonic setting of Taiwan (Peng and Chao, 2008). Additionally, the stress drops estimated from the vein lengths and shear offsets across foliation-parallel veins are between 10-100 MPa (Figure 14), an order of magnitude or more higher than stress drops estimated for seismic tremor (e.g. Fletcher and McGarr, 2011). Higher stress drops calculated for the veins are likely biased by discontinuous outcrop exposure, leading to underestimated vein length measurements. Alternatively, low stress drops of tectonic tremor/VLFEs may be representative of incremental opening (i.e. tremor bursts), which would mean the offsets measured here are total offsets of many events. In summary, the foliation sub-parallel shear fractures described here

formed in a different tectonic setting to observed tremor, but the shear fracture mechanism and conditions of failure they record could be comparable to the mechanism that is important to the tremor source, because the mixed rheology recorded by the veins is similar to inferred conditions for tremor and VLFEs. Fluctuations in differential stress and fluid pressure could promote the nucleation of brittle fractures in the ductile regime.

### 2.8. Conclusion

This study aimed to 1) provide a mechanical interpretation for the formation of foliation-parallel shear fractures within a ductile shear zone, and 2) compare the conditions under which these structures formed to those where tremor is observed today. I have presented a combination of outcrop-scale observations and microstructural analyses that were used to constrain the physical conditions at which these structures formed and subsequently deformed. The observation of shear fractures subsequently folded and boudinaged indicates a coeval brittle-ductile deformation system. Using microstructural observations of host rock assemblages and dynamic recrystallization of quartz veins, I conclude ductile deformation occurred at temperatures 380-500°C. Fluid inclusion thermobarometry of secondary fluid inclusion assemblages, formed post-crystallization of the vein, reflects trapping temperatures of 515-680°C and 320-400°C. Geochemical data indicates veins precipitated from magmatic and meteoric fluids, suggesting the presence of fluids during all phases of shear zone deformation. Average grain sizes calculated by EBSD reflect flow stresses between ~60 and ~87 MPa (Stipp and Tullis, 2003). These stresses are greater than the cohesive strength of similar rocks, suggesting the formation of shear fractures occurs as a result of increased differential stress and high pore pressure as opposed to major stress-reorientation as a result of an earthquake.

Our new data have some consistencies with all previously published models. Because the source parameters of tectonic tremor remain undefined, the physical structures produced by tectonic tremor in the rock record are still unidentified. Nevertheless, this study has emphasized the similarities between the formation conditions of these structures to the characteristics of tectonic tremor. Nucleation of brittle fractures as a result of fluctuating differential stress and fluid pressure during shear zone deformation may represent similar mechanisms to VLFEs and tectonic tremor.

# TABLES

## Table 1. Results from stable isotope geochemistry

*Table I. Stable isotope results*

| | T (°C) | Mineral | $\delta^{18}O$ | $\delta D$ | Description |
|---|---|---|---|---|---|
| KC 1-1* | 400°C | quartz | 7.235 | | shear fracture vein, 3rd oldest |
| KC 1-2 | 400°C | quartz | 7.708 | | |
| KC 2-1* | 400°C | quartz | 5.212 | | 2nd oldest vein in outcrop |
| KC 2-2 | 400°C | quartz | 6.3 | | |
| KC 2-3 | 400°C | quartz | 5.258 | | |
| KC 2-4 | 400°C | quartz | 2.458 | | |
| KC 3-1* | 400°C | quartz | 4.202 | | youngest vein in the outcrop |
| KC 3-2 | 400°C | quartz | 2.458 | | |
| KC 3-3 | 400°C | quartz | 3.493 | | |
| KC 4-1* | 400°C | tourmaline | 8.314 | -92.557 | 2nd youngest vein in outcrop, tightly folded |
| KC 4-2 | 400°C | tourmaline | 6.85 | | |
| KC 4-3 | 400°C | tourmaline | 7.779 | | |
| KC 5-1* | 400°C | tourmaline | 8.06 | -95.485 | oldest vein in outcrop, heavily folded |
| KC5-2 | 400°C | tourmaline | 7.711 | | |

* most precise runs

FIGURES

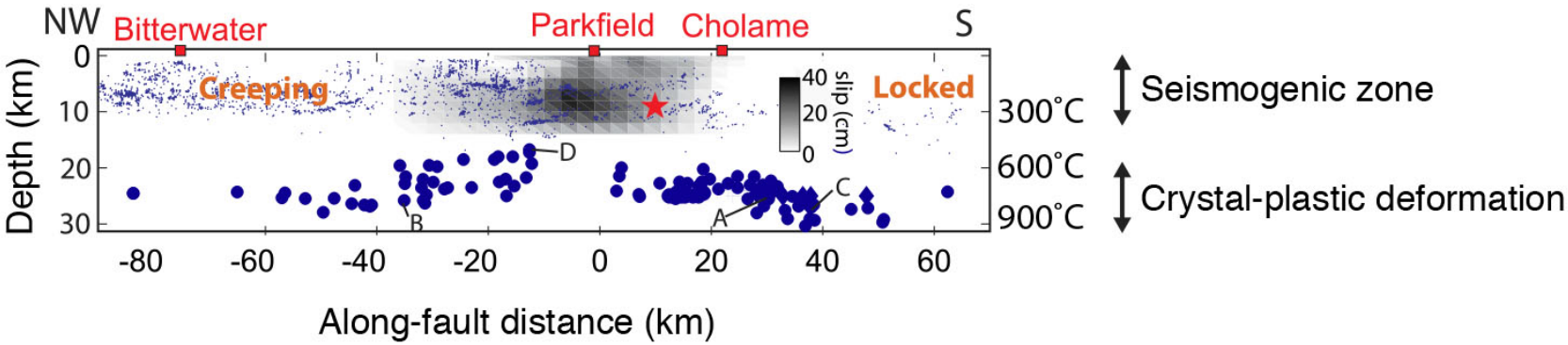


Figure 1. Depths of tectonic tremor along the San Andreas fault in California, modified from *Shelly and Hardebeck* (2010). Tectonic tremor is observed between 18-40 km depth along this transform fault, consistent with temperatures between 500-1000°C. At these temperatures, crystal-plastic deformation is expected to dominate for quartzo-feldspathic rocks (Stipp *et al.*, 2002).

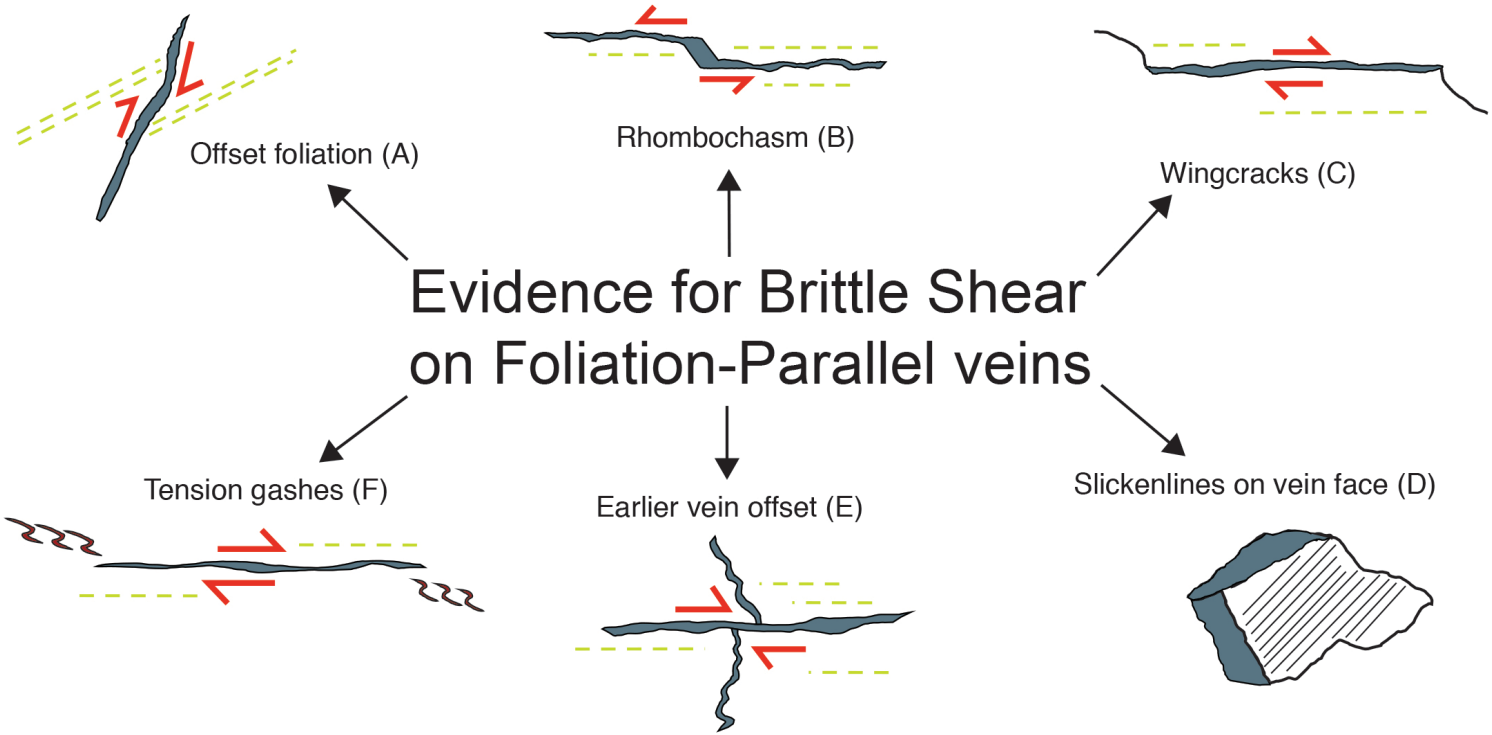


Figure 2. Proposed kinematic indicators recording shear offset across veins in shear zones. Structures proposed include (A) offset foliations; (B) rhombochasm or opening-mode structures, forming polygonal openings as a result of shear; (C) wing cracks, which form as tensile cracks at the propagation tip of shear failures; (D) slickenlines on the vein face, indicating direction of shear; (E) physical offset of earlier-formed veins that cut the foliation along shear fractures; (F) tension gashes at the tip of shear failures, exhibiting a sigmoidal shape consistent with the direction of shear

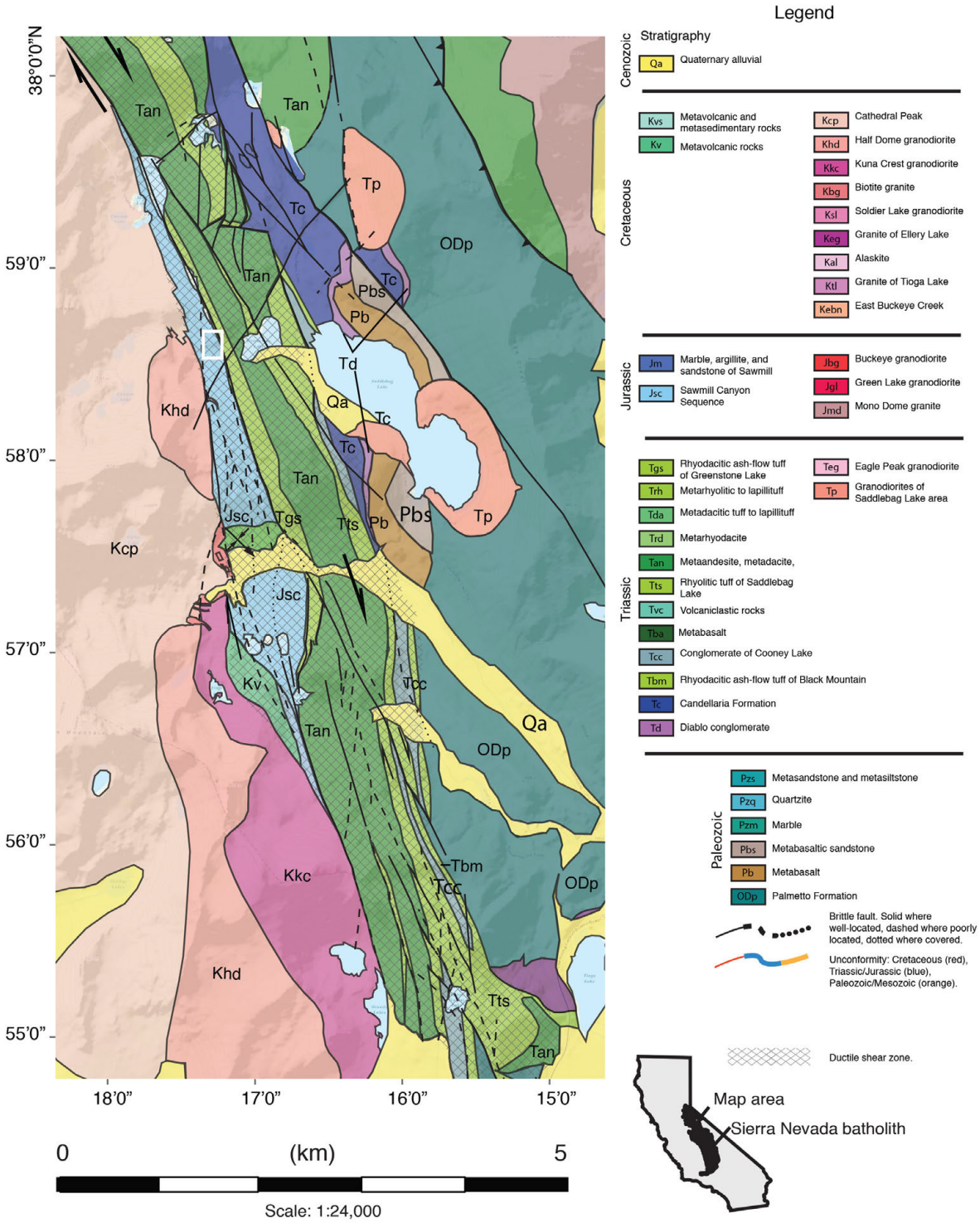


Figure 3. Geologic map of the Steelhead Lake shear zone, adapted from Hartman (in preparation). The Steelhead Lake shear zone is well defined along the eastern boundary of the Tuolumne Intrusive Complex ($K_{hd}$, $K_{cp}$, $K_{kc}$). Black lines show late-stage brittle faults that cut the shear zone.

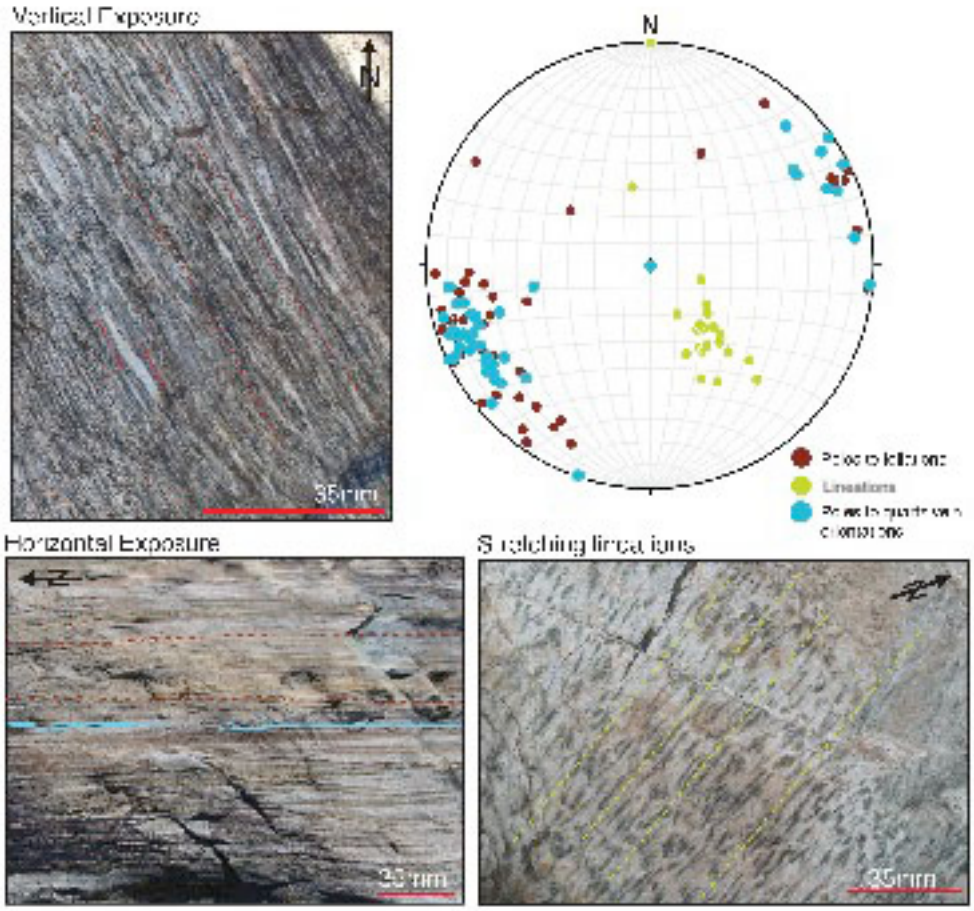


Figure 4. Structural measurements represented on a stereonet plot. Measurements correspond to structures observed in vertical and horizontal surfaces. Steep lineations, transposed bedding, and sheared clasts and lenses reflect tranpressional strain. Red dotted lines indicate orientations of foliation measurements. Solid blue lines in the horizontal exposure indicate orientation of a thin quartz vein. Dotted green lines indicate orientation of lineations, defined by elongated diopside grains.

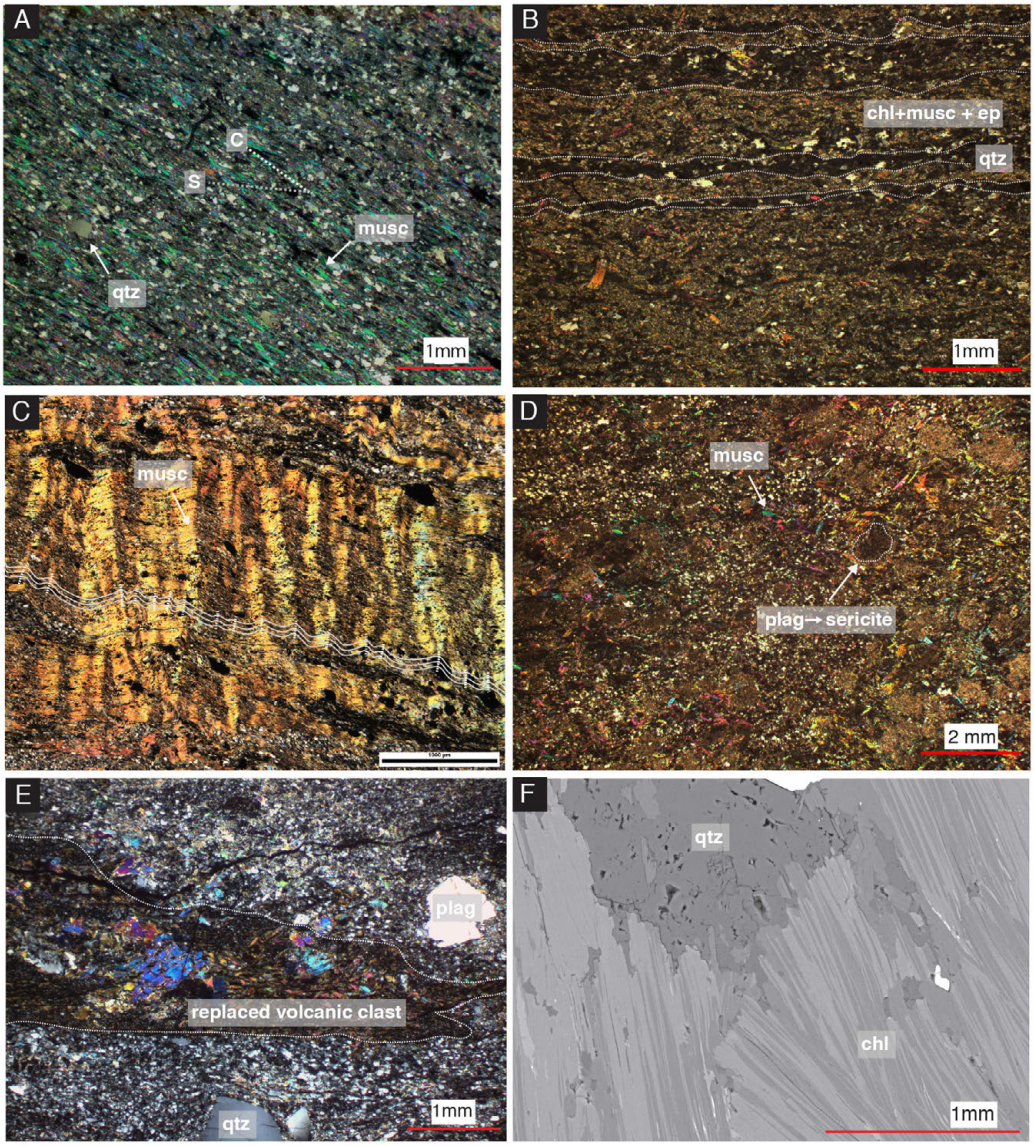


Figure 5. Photomicrographs of host rock assemblages. (A) Silicate-rich Jurassic metasedimentary subunit, with a foliation defined by the alignment of elongated chlorite and muscovite grains. (B) Calc-silicate subunit of the Jurassic metasedimentary sequence. Foliation of this subunit is defined by the banding of quartz and chlorite and epidote rich zones. This assemblage also contains diopside. (C) Triassic andesite metavolcanic unit exhibiting a folded foliation. The foliation in this rock is defined by elongated muscovite grains. Axial planes of crenulation cleavage folds are indicated on the photomicrograph. (D) Triassic andesite host rock assemblage, with plagioclase phenocrysts that have been completely altered to very fine-grained sericite. Muscovite bends around altered phenocrysts. (E) Triassic rhyolite sample with a volcanic clast altered to muscovite, chlorite, and fine-grained rutile grains. The weak foliation of the rock is due to the lack of elongated grains. Large plagioclase and quartz phenocrysts remain unaltered in the host rock. (F) SEM back scattered electron (BSE) image of chlorite grains in the Jurassic calc-silicate.

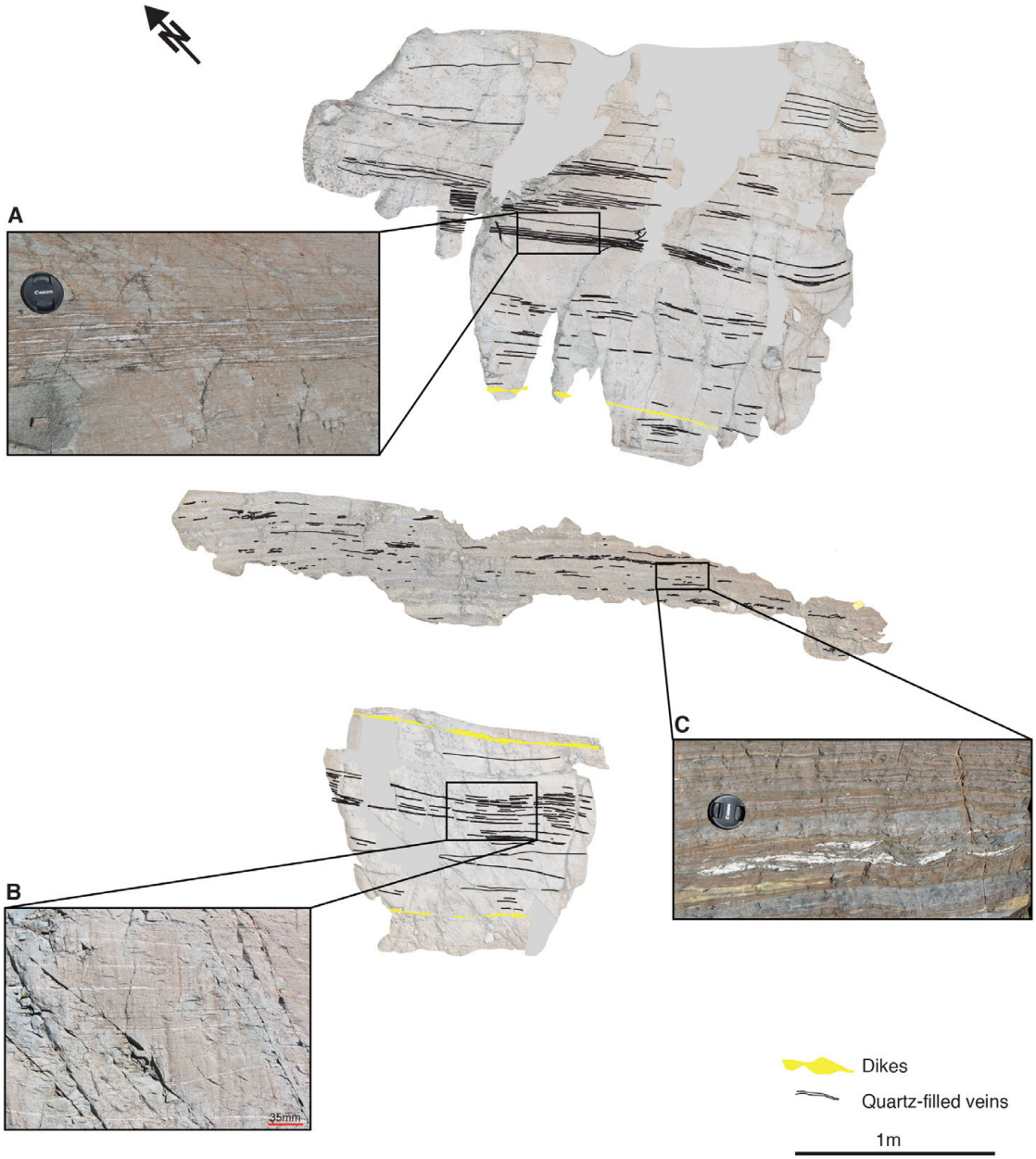


Figure 6. Outcrop-scale map of three flat exposures. White space in between outcrops is covered ground. Location of outcrop is marked by the white rectangle in Figure 3. Middle outcrop is composed of the more calc-rich metasedimentary unit, while the remaining two outcrops consist of the silicate-rich member. Quartz veins in exposures A and B are parallel to the foliation of the rock and in some areas are found spaced every ~10 mm. The veins fold with the foliation slightly. Veins in outcrop C are heavily deformed; the veins appear to be transposed and folded twice. Lenses are sheared. Banding in this outcrop is obvious.

A
35 mm

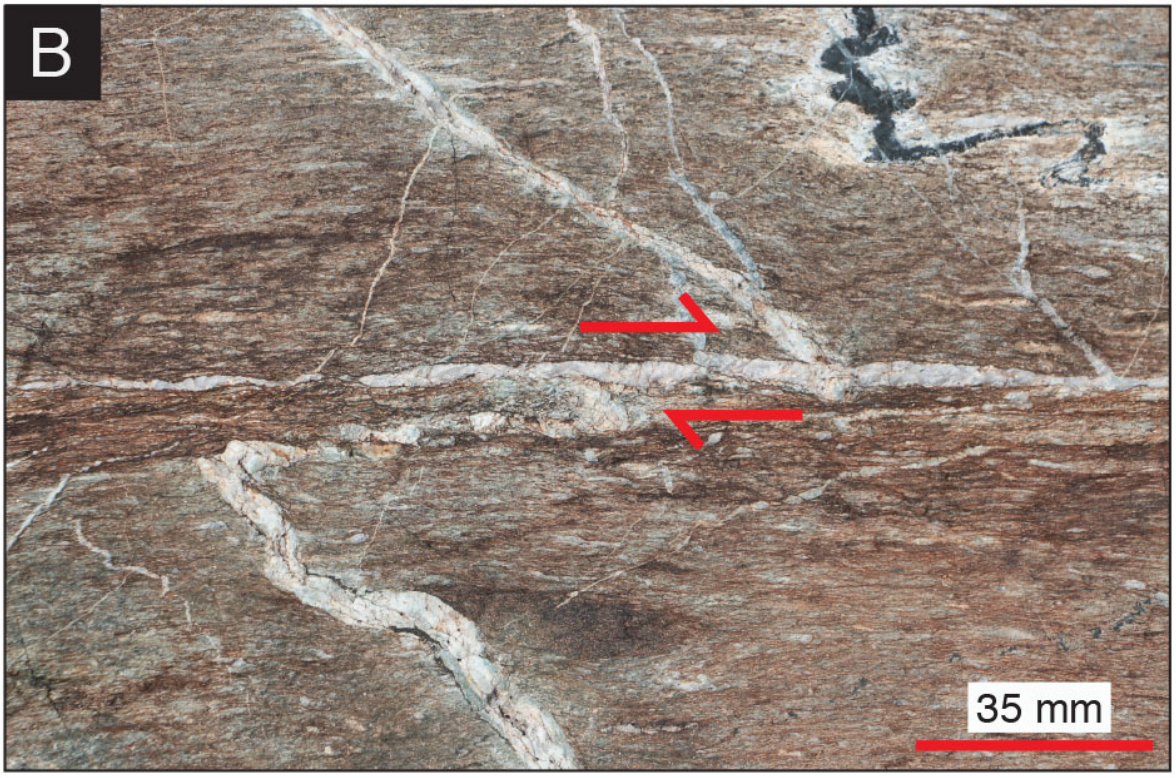
B
35 mm

Figure 7 (previous page). Vein deformation in outcrop, recording shear offset in foliation-parallel veins. (A) Rhombochasm structure exhibiting dextral offset. (B) Shear fracture vein parallel to the foliation of the host rock. Offset of an older vein indicates dextral offset. Shear fracture vein is slightly boudinaged and the older vein is folded.

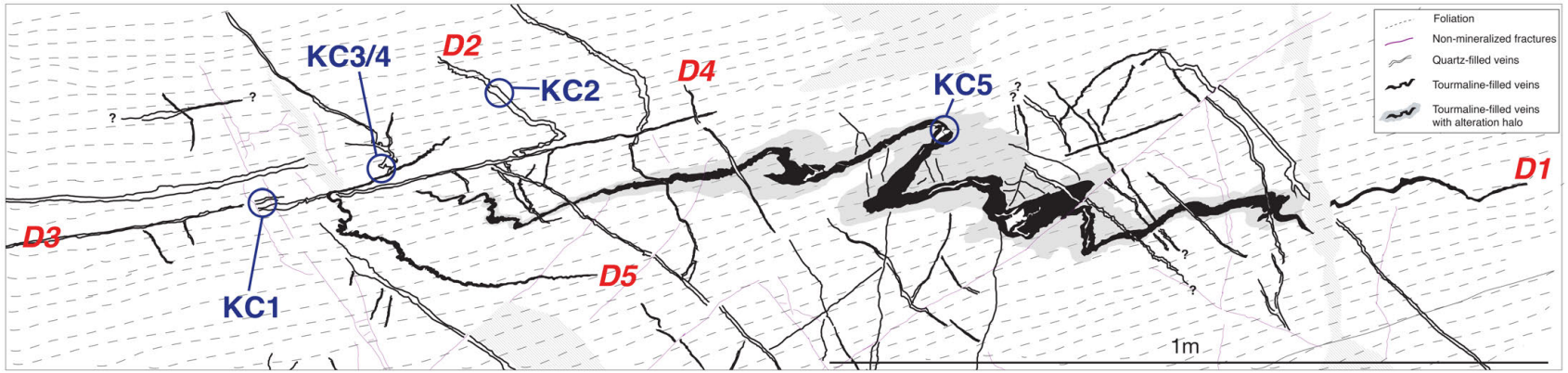


Figure 8. Outcrop-scale map of vein deformation in the silicate-rich Jurassic unit. This outcrop contains 5 sets of veins. A chronological order of vein formation can be pieced together with crosscutting relationships of these veins. The oldest vein in this outcrop, is the large tourmaline vein, which cuts the foliation (D1). This vein has been transected by a series of thin quartz veins, which also cut the foliation (D2). Shear offset of D2 veins are seen along the foliation-parallel quartz vein (D3). A small quartz vein (D4) cuts the foliation, crossing both D3 and D1 veins. Lastly, a very thin tourmaline vein cuts D2 veins (D5). This vein is tightly folded. Red labels indicate deformation events. Blue labels note the veins from which samples were taken for isotope analysis.

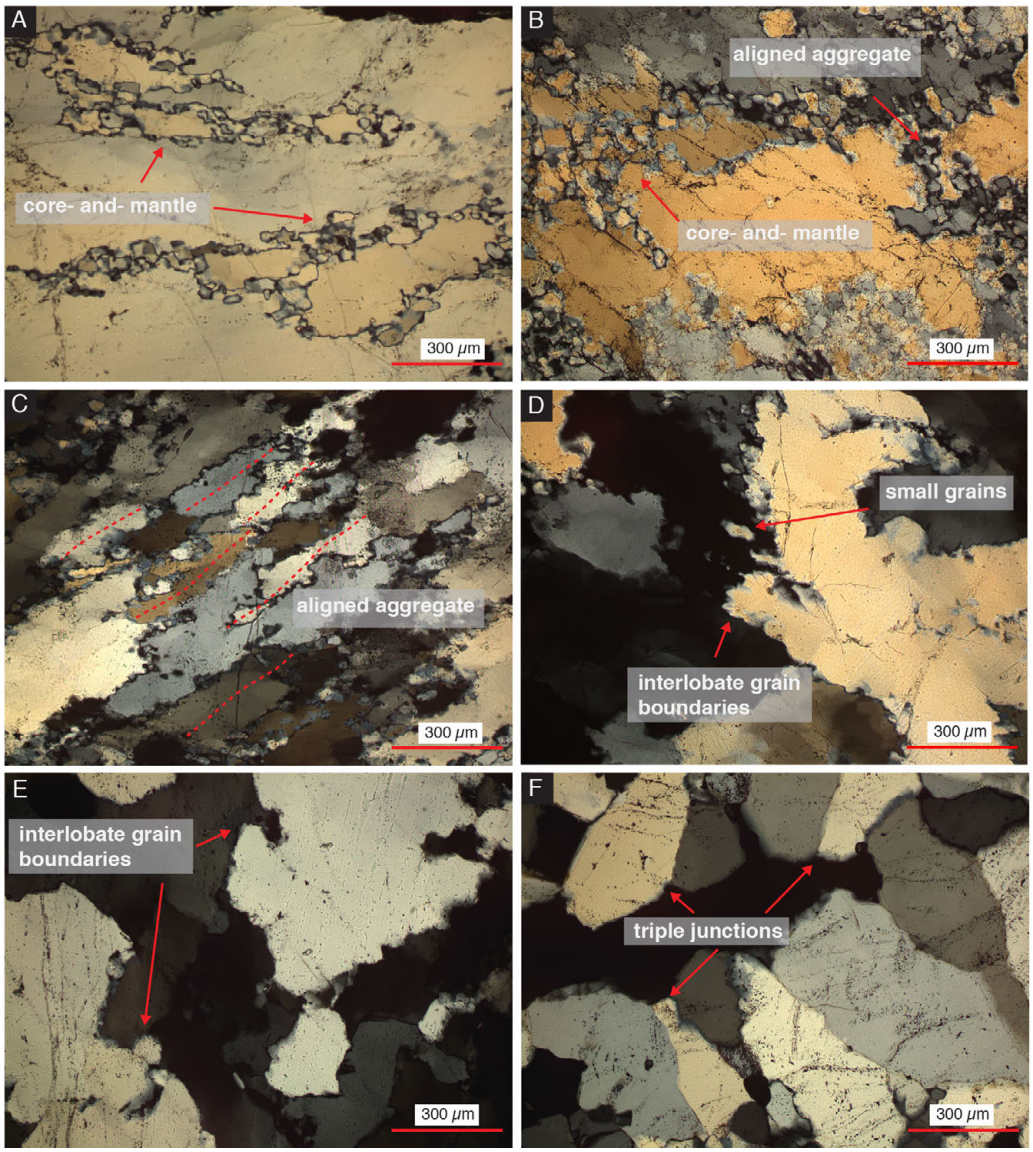


Figure 9. Microstructural characteristics of foliation sub-parallel quartz veins (A) Group 1, consistent with bulging recrystallization (BLG). Small, recrystallized subgrains line the boundaries of large, original quartz grains. Larger grains exhibit patchy extinction. Fluid inclusions are visible across multiple grain boundaries. (B) Intermediate Texture #1, including both a core- and- mantle structure (consistent with Group 1) and smaller, elongated subgrains (consistent with Group 2). (C) Group 2, representative of subgrain rotation recrystallization (SGR). Grains are more elongated and small subgrains are larger. An alignment of the long axes of all grains is visible. The orientation is at an angle to the orientation of the vein itself. (D) Intermediate Texture #2; this group is defined by the presence of both smaller, elongated grains and an interlobate aggregate, consistent with observations from Groups 2 and 3. (E) Group 3, consistent with grain boundary migration recrystallization (GBM). This group is defined by large, interlobate grains with little to no subgrains. (F) Statically recrystallized quartz, characterized by uniform extinction, lack of subgrains, and triple junction grain boundaries.

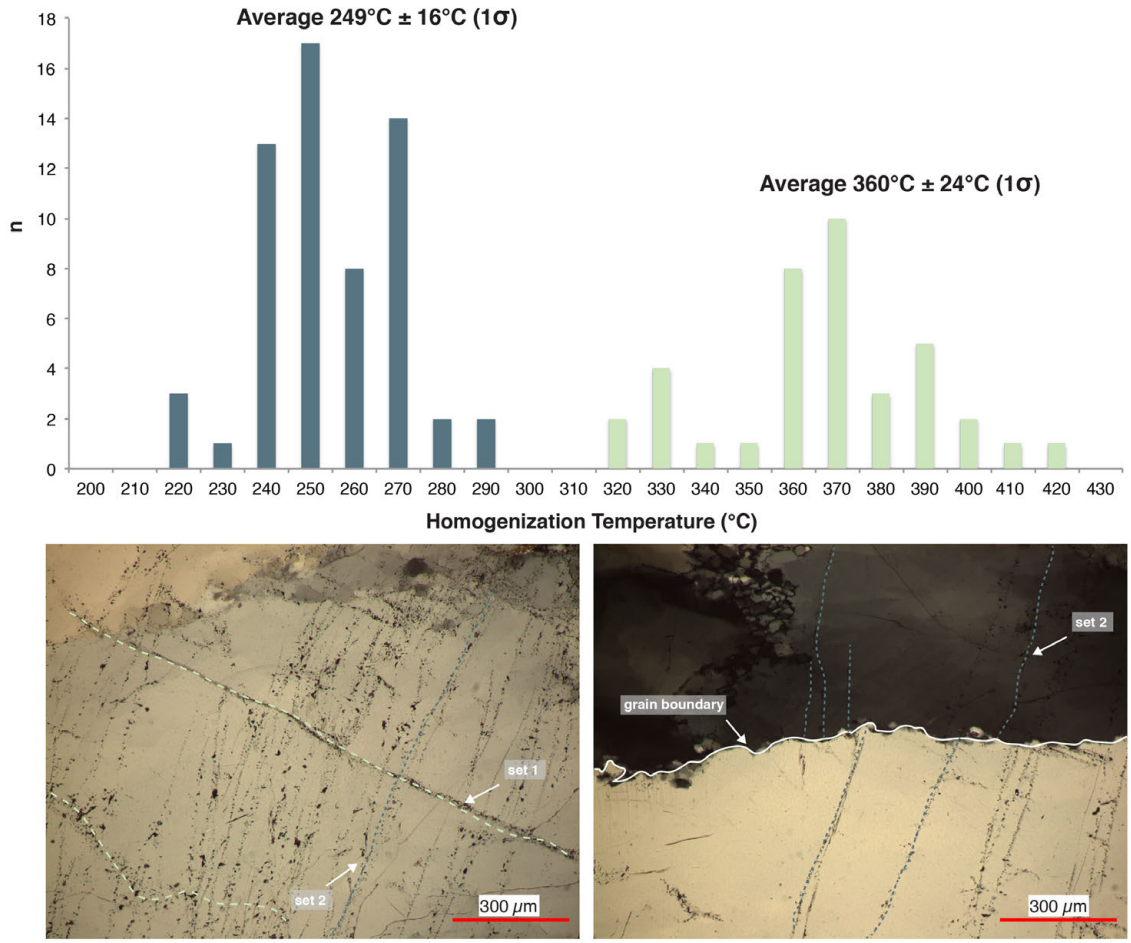


Figure 10. Frequency distribution of fluid inclusion homogenization temperatures. Two unique fluid inclusion trails are represented in the bi-modal distribution of these homogenization temperatures. Set 1 planes propagate across the entire vein and appear unaffected by grain boundaries (lower left). Set 2 planes are linear and terminate at grain boundaries formed by dynamic recrystallization of the vein (lower left and lower right).

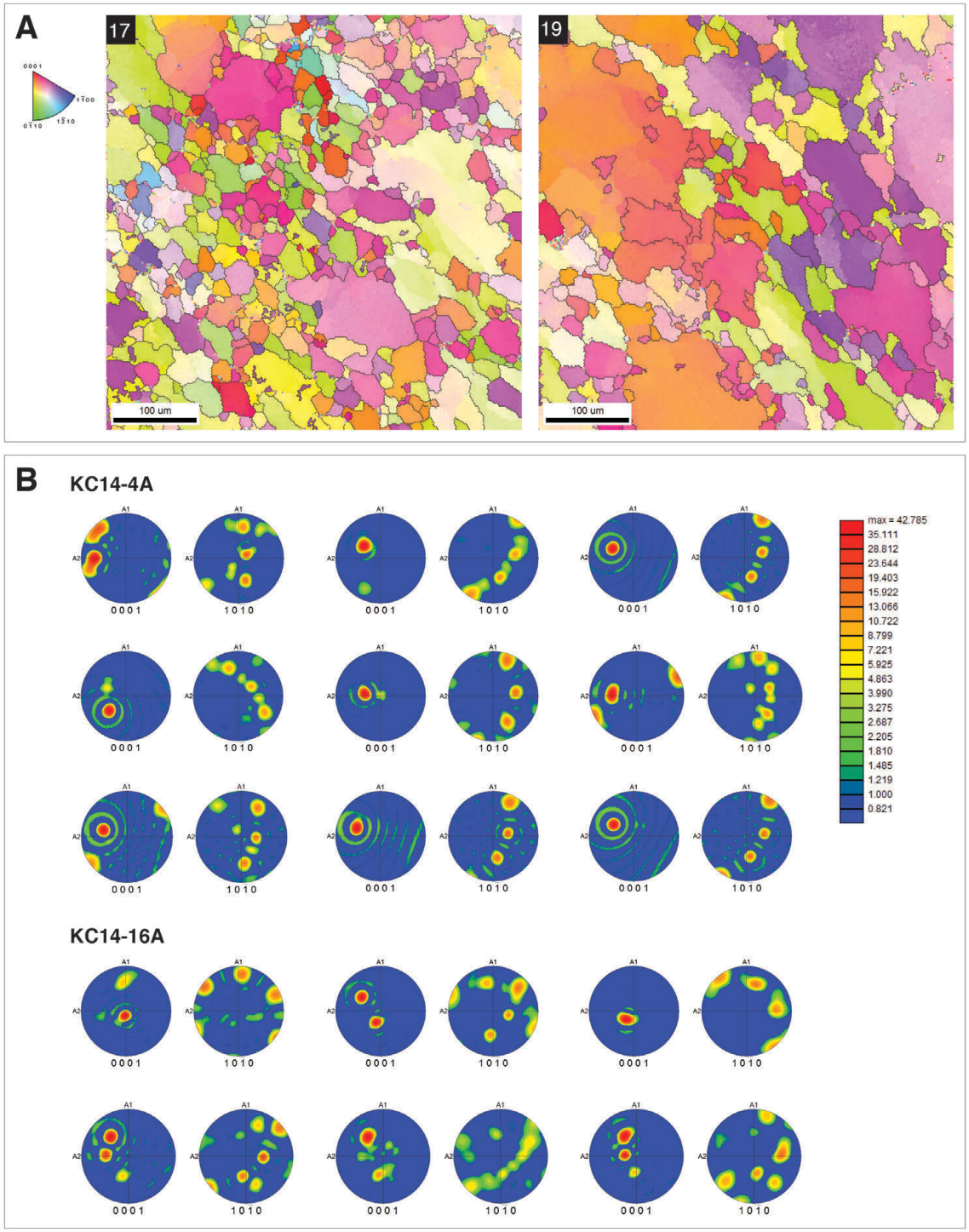
A
17
19
100 um
100 um
B
KC14-4A
KC14-16A
A1
A2
0001
1010
max = 42.785
35.111
28.812
23.644
19.403
15.922
13.066
10.722
8.799
7.221
5.925
4.863
3.990
3.275
2.687
2.205
1.810
1.485
1.219
1.000
0.821

Figure 11 (previous page). Results from electron backscatter diffraction (EBSD). Samples used were cut in the direction perpendicular to the foliation and parallel to the lineation. Indexed maps (A) indicate both grain size distribution and grain orientation. Scans 17 and 19 were taken at a 2 μm step-size over a 500x500 μm area within a foliation-parallel quartz vein. Both scans were taken from the same sample (16A). Quartz c- and a- axes pole figure intensity plots (B) for scans across two samples indicate a fairly consistent c-axis orientation across each sample. Variations in a-axes are observed between samples.

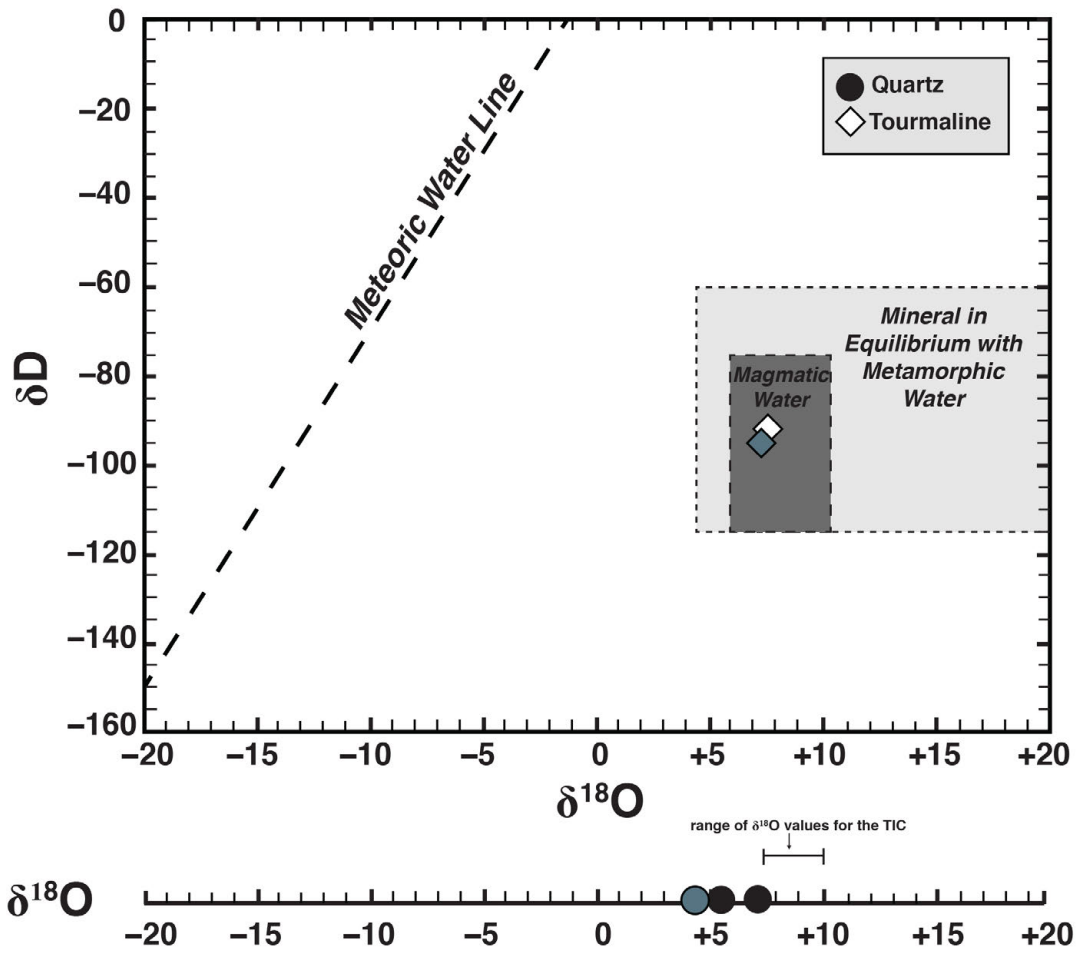


Figure 12. Results from stable isotopic geochemistry, analyzed in the California State University Long Beach IIRMES lab. Hydrogen analyses were not run on quartz samples. Because of this, they are plotted on a separate axis. Blue symbols indicate samples deriving from the same vein (KC3, KC4). Tourmaline hydrogen and oxygen values are consistent with known values for magmatic waters. Quartz oxygen values are lower than the accepted range of values for magmatic waters, and lower than the range of $\delta^{18}O$ values for the Tuolumne Intrusive Complex. Data from Magaritz and Taylor (1976), Kistler *et al.* (1989), and Lackey *et al.* (2008).

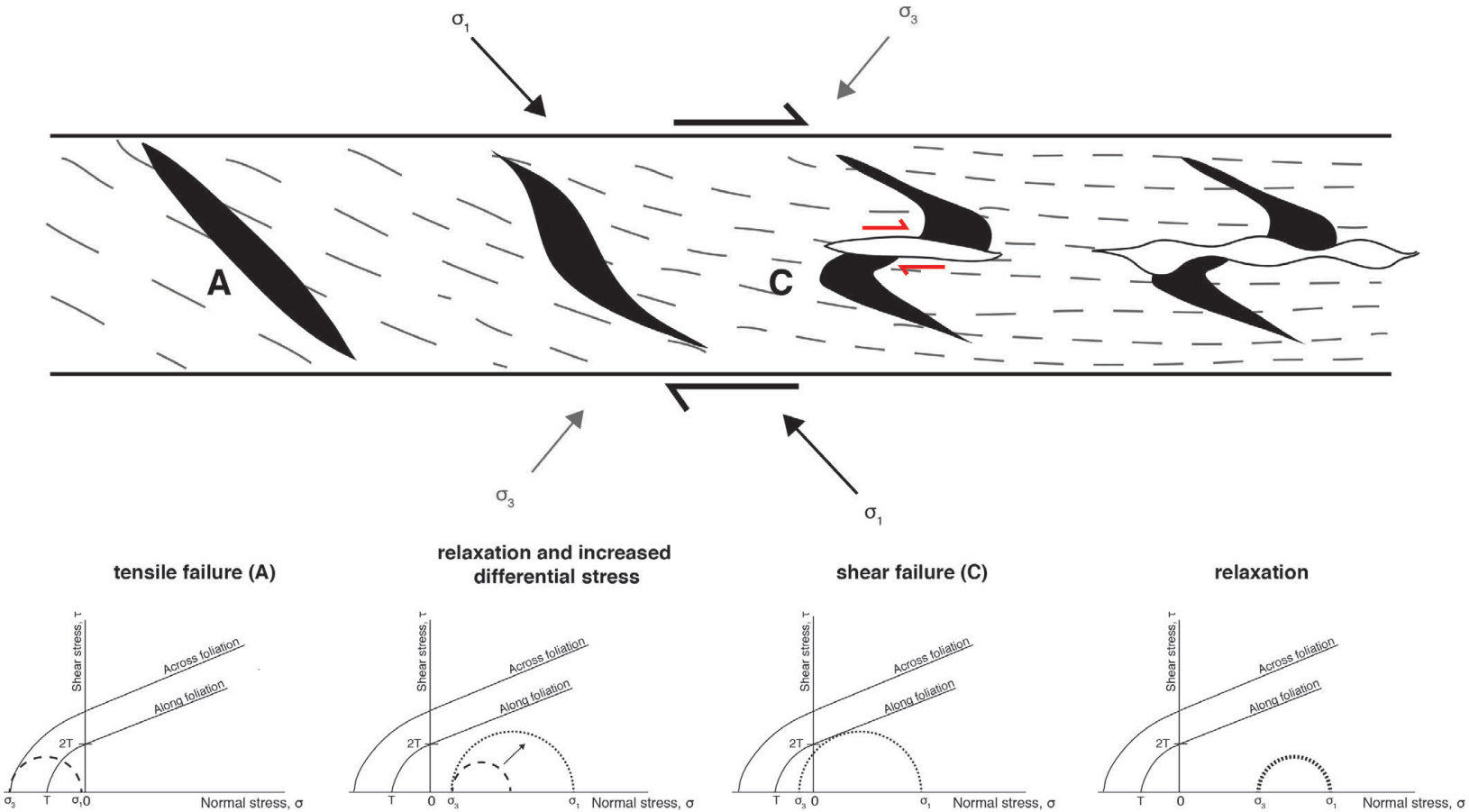


Figure 13 (previous page). Vein deformation in a shear zone, modified after *Kerrich and Allison* (1978). Mohr circle diagrams beneath each deformation episode represent the interpreted stress field during at each stage of the shear zone deformation. Older veins most likely formed as tensile fractures cutting the weak foliation of the rock under a lower differential stress. Post-failure, pore pressure decreased and differential stress decreased. Over time, increased pore pressures and increased differential stress drive the system to shear failure. Mode II cracks form along the foliation of the rock.

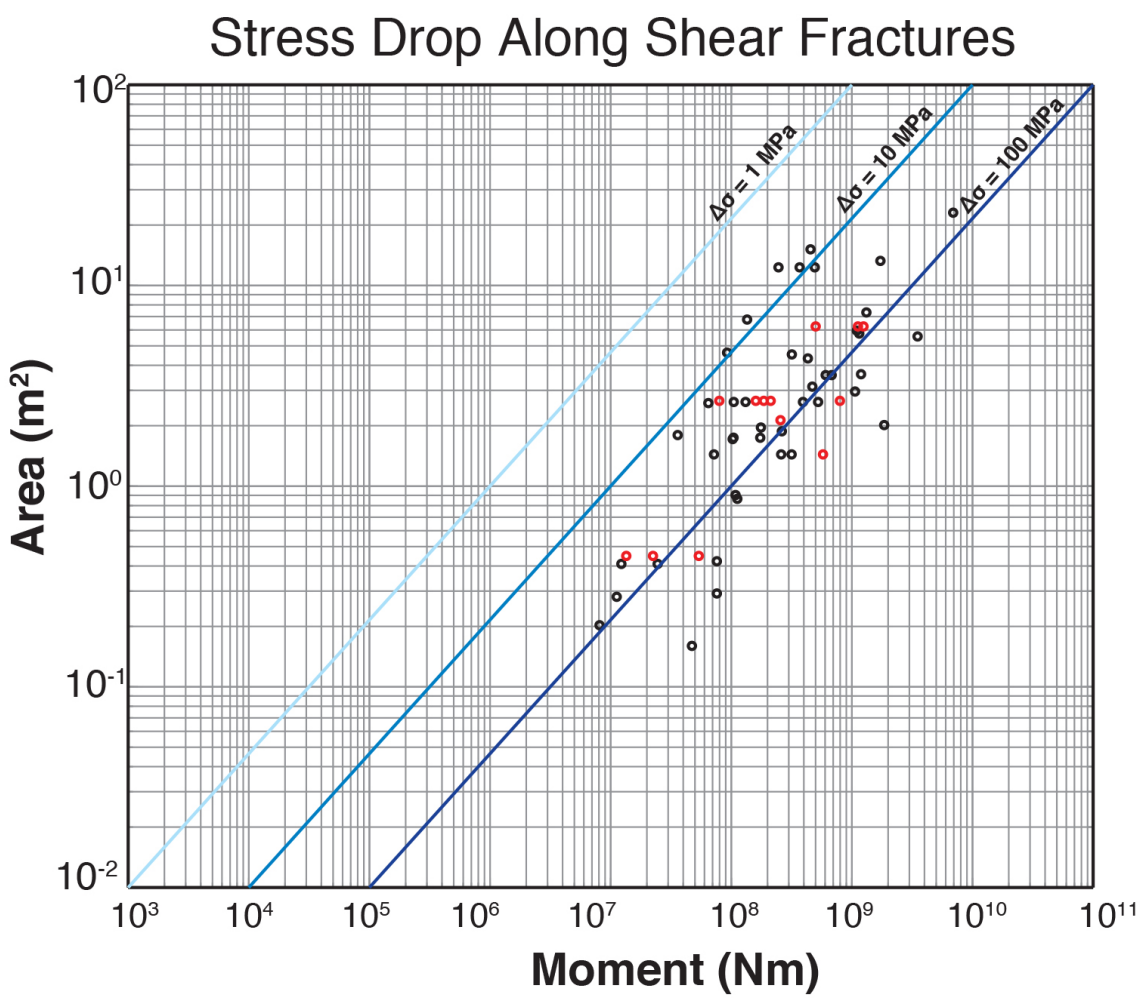


Figure 14. Stress drops of shear fractures in the study area, calculating by plotting the areas (area= $L^2$) against the seismic moments. Seismic moments were calculated by $M_o = \mu(L^2 * D)$, where L is length of the quartz vein, D is shear offset or displacement along the vein, and $\mu$ is the shear modulus, assumed to be $1 \times 10^9$. These calculated values are an order of magnitude higher than stress drops of tectonic tremor. Red markers indicate veins which lengths could not be measured in full.

# CHAPTER 3

Future work on this project may be able to more tightly constrain the potential relationship between these shear structures and seismic tremor. I suggest expanding the microstructural and geochemical datasets, considering different field areas, and modeling the effect of strain accumulation of heterogeneous units within a shear zone.

In this project, I collected data from a variety of sources. However, the electron backscatter diffraction and stable isotope datasets could be enhanced. With the present dataset, the isotope data is consistent with a magmatic tourmaline source and a nonmagmatic quartz source. However, only five samples were run for oxygen isotope analysis, so trends in the data cannot be interpreted. To be able to use the isotope data to more confidently assess the fluid history of the shear zone, I suggest collecting more samples from outcrops exhibiting the same brittle-ductile deformation studied in this project. Samples should be taken from outcrops ranging in distance from the pluton boundary. Multiple runs of these samples would increase the accuracy of the dataset as well. In this project, we did not run hydrogen isotope analyses on quartz samples, because we believed the fluid inclusions formed post-crystallization of the quartz. Running both oxygen and hydrogen analyses on quartz veins with fluid inclusions which show characteristic of primary inclusion formation, in collaboration with hydrogen and oxygen of tourmaline veins in the same outcrop, would help tightly constrain the temperature. Further work using electron backscatter diffraction would solidify the grain size measurement dataset, which would be helpful in increasing the confidence level of inferred flow stresses. The study of grain size distribution over a range of recrystallization mechanisms (BLG, SGR, and GBM) would provide insight into the levels of stress over shear zone deformation. The grain sizes we

estimated from EBSD are from relatively small areas of the vein, and thus may not be representative of the entire population of quartz veins. However, the grain sizes were used to place an order of magnitude constraint on the flow stress. The analysis of more samples would increase the confidence in the data, as only one sample was analyzed at the highest quality in this study. A continuation of the fluid inclusion analysis would increase the accuracy of the dataset. Four samples were used for fluid inclusion analysis in this study; an increase in the number of samples analyzed from locations across the shear zone would provide a more complete conclusion. Further, an increased number of freezing point depression measurements would increase the confidence in the dataset.

The second thing I would expand on for this project is data from other field areas. This study focused on a shear zone bound by a magmatic intrusion. Through our work, we maintain that the shear zone would have deformed similarly if the TIC did not exist. In order to prove that these structures form in other shear zones, I suggest further fieldwork in other exhumed shear zones along transform faults that are not bound by batholiths or plutons.

The models presented by *Hayman and Lavier* (2014) and *Fagereng* (2014) propose brittle structures form in shear zones as a result of heterogeneity in the rheology of the rocks. In the *Hayman and Lavier* (2014) model, brittle fractures form in rigid lenses surrounded by a less rigid medium. It would be interesting to model this kind of heterogeneous system in the lab to understand what amount of strain accumulation leads to failure, and what temperatures are consistent with the nucleation of fractures.

# REFERENCES


Aiken, C. Peng, Z. & Chao, K., 2013. Tremor along the Queen Charlotte Margin triggered by large teleseismic earthquakes. Geophysical Research Letters v. 40, p. 829-834.

Ague, J.J., & Brimhall, G.H., 1988. Magmatic arc asymmetry and distribution of anomalous plutonic belts in the batholiths of California: effects of assimilation, crustal thickness, and depth of crystallization. Geological Society of America Bulletin, v. 100, p. 912-927.

Albertz, M., Paterson, S.R., & Okaya, D., 2005. Fast strain rates during pluton emplacement: Magmatically folded leucocratic dikes in aureoles of the Mount Stuart Batholith, Washington, and the Tuolumne Intrusive Suite, California. Geological Society of America Bulletin, v. 117, p. 450-465.

Albertz, M., 2006. Relationships between melt-induced rheological transitions and finite strain: observations from host rock pendants of the Tuolumne Intrusive Suite, Sierra Nevada, California. Journal of Structural Geology, v. 28, p. 1422-1444.

Barth, A.P., Walker, J.D., Wooden, J.L., Riggs, N. R., & Schweickert, R. A., 2011. Birth of the Sierra Nevada magmatic arc: Early Mesozoic plutonism and volcanism in the east-central Sierra Nevada of California. Geosphere, v. 7, p. 877-897.

Bateman, P.C., 1992. Plutonism in the Central Part of the Sierra Nevada Batholith, California. U.S. Geological Survey Professional Paper, 1483, 186 p.

Beaudoin, G. & P. Therrien. 1999-2015, AlphaDelta Stable Isotopes Fractionation Calculator, http://www2.ggl.ulaval.ca/cgi-bin/alphadelta/alphadelta.cgi (Accessed June 2015)

Behr, W.M., & Platt, J.P., 2011. A naturally constrained stress profile through the middle crust in an extensional terrane. Earth and Planetary Science Letters, v. 303, p. 181-192.

Platt, J.P., & Behr, W. M., 2011. Lithospheric shear zones as constant stress experiments. Geology, v. 39, p. 127-130.

Beroza, G.C., & Ide, S., 2011. Slow earthquakes and nonvolcanic tremor. Annual review of Earth and Planetary Sciences, v. 39, p. 271-296.

Bodnar, R.J., Binns, P.R., & Hall, D.L., 1989. Synthetic fluid inclusions-VI. Quantitative evaluation of the decrepitation behaviour of fluid inclusions in quartz at one atmosphere confining pressure. Journal of Metamorphic Geology, v. 7, p. 229-242.

Bodnar, R.J., 2003. Reequilibration of fluid inclusions. In: Samson, I., Anderson, A., Marshall, D. (Eds.), Fluid Inclusions: Analysis and Interpretation. Short Course, 32. Mineralogical Association of Canada, pp. 213-230.

Brace, W.F., & Kohlstedt, D.L., 1980. Limits on lithospheric stress imposed by laboratory experiments. Journal of Geophysical Research: Solid Earth, v. 85, p. 6248-6252.

Brook, C.A., 1977, Stratigraphy and structure of the Saddlebag Lake roof pendant, Sierra Nevada, California: Geological Society of America Bulletin, v.88, p.321-334.

Brook, C.A., Nokleberg, W. J., & Kistler, R. W., 1974. Nature of the angular unconformity between the Paleozoic metasedimentary rocks and the Mesozoic metavolcanic rocks in the eastern Sierra Nevada, California. Geological Society of America Bulletin, v. 85, p. 571-576.

Brook, C.A., 1977. Stratigraphy and structure of the Saddlebag Lake roof pendant, Sierra Nevada, California. Geological Society of America Bulletin, v. 88, p. 321-334.

Burlini, L., Di Toro, G., & Meredith, P., 2009. Seismic tremor in subduction zones: Rock physics evidence. Geophysical Research Letters, 36, L08305.

Cao, W., Paterson, S., Memeti, V., Mundil, R., Anderson, J. L., & Schmidt, K., 2015. Tracking paleodeformation fields in the Mesozoic central Sierra Nevada arc: Implications for intra-arc cyclic deformation and arc tempos. Lithosphere, L389.1.

Chamberlain, C.J., Shelly, D.R., Townend, J., & Stern, T.A., 2014. Low-frequency earthquakes reveal punctuated slow slip on the deep extent of the alpine fault, New Zealand. Geochem., Geophys., Geosyst., v. 15, p. 2984 -2999.

Chao, K., Peng, Z., Gonzalez-Huizar, H., Aiken, C., Enescu, B., Kao, H., Velasco, A.A., Obara, K., Matsuzawa, T., 2013. A global search for triggered tremor following the 2011 $M_w$ 9.0 Tohoku Earthquake. Bull. Seismol. Soc. Am. 103, 1551-1571.

Dunne, G. C., & Walker, J. D., 2004. Structure and evolution of the East Sierran thrust system, east central California. Tectonics, v. 23, TC4012, 23 p.

Etheridge, M.A., 1983. Differential stress magnitudes during regional deformation and metamorphism: Upper bound imposed by tensile fracturing. Geology, v. 2, p. 231-234.

Fagereng, Å., Remitti, F., & Sibson, R. H., 2011. Incrementally developed slickenfibers - Geological record of repeating low stress-drop seismic events? Tectonophysics, v. 5, p. 381-386.

Fagereng, Å., Hillary, G.W., & Diener, J. F., 2014. Brittle-viscous deformation, slow slip, and tremor. Geophysical Research Letters, v. 41, p. 4159-4167.

Fisher, D.M., Brantley, S.L., Everett, M., & Dzvonik, J., 1995. Cyclic fluid flow through a regionally extensive fracture network within the Kodiak accretionary prism. Journal of Geophysical Research, v. 100, p. 12,881-12,794.

Fletcher, J.B., & McGarr, A., 2011. Moments, magnitudes, and radiated energies of non-volcanic tremor near Cholame, CA, from ground motion spectra at UPSAR. Geophysical Research Letters, 38, L16314.

Gifkins, R., 1976. Grain-boundary sliding and its accommodation during creep and superplasticity. Metallurgical Transactions A, v. 7, p. 1225-1232.

Greene, D.C., & Schweickert, R. A., 1995. The Gem Lake shear zone: cretaceous dextral transpression in the northern Ritter Range Pendant, eastern Sierra Nevada, California. Tectonics, v. 14, p. 945-961.

Hall, D.L. & Wheeler, J.R., 1992. Fluid composition and the decrepitation behavior of synethic fluid inclusions in quartz. Pan American Conference on Research on Fluid Inclusions, Program and Abstracts, 39.

Hartman, S., 2013. Transitional ductile to brittle strike-slip rheology: An exhumed laboratory of the seismogenic zone in the eastern central Sierra Nevada, California. Geological Society of America *Abstracts with Programs*, 45(7), 830.

Hayman, N.W., & Lavier, L.L., 2014. The geologic record of deep episodic tremor and slip. *Geology*, v. 42, p. 195-198.

Hanson, R.B., Sorensen, S.S., Barton, M. D., & Fiske, R. S., 1993. Long-term evolution of fluid–rock interactions in magmatic arcs: evidence from the Ritter Range pendant, Sierra Nevada, California, and numerical modeling. *Journal of Petrology*, v. 34, p. 23-62.

Henderson, I.H.C., & McCaig, A. M., 1996. Fluid pressure and salinity variations in shear zone-related veins, central Pyrenees, France: implications for the fault-valve model. *Tectonophysics*, v. 262, p. 321-348.

Hirth, G., & Tullis, J., 1992. Dislocation creep regimes in quartz aggregates. *Journal of Structural Geology*, v. 14, p. 145-159.

Hirth, G., & Tullis, J., 1994. The brittle-plastic transition in experimentally deformed quartz aggregates. *Journal of Geophysical Research: Solid Earth (1978–2012)*, v. 99, p. 11731-11747.

Hirose, H., & Obara, K., 2006. Short-term slow slip and correlated tremor episodes in the Tokai region, central Japan. *Geophysical Research Letters*, *33*(17).

Hobbs, B.E., Ord, A., & Teyssier, C., 1986. Earthquakes in the Ductile Regime? Pure and Applied Geophysics, v. 124, p. 309-336.

Hodgson, C. J.,1989. The structure of shear-related, vein-type gold deposits: a review. Ore Geology Reviews, v. 4, p. 231-273.

Ide, S., Shelly, D. R., & Beroza, G. C., 2007. Mechanism of deep low frequency earthquakes: Further evidence that deep non-volcanic tremor is generated by shear slip on the plate interface. Geophysical Research Letters, 34.3.

Ito, Y., & Obara, K., 2006. Very low frequency earthquakes within accretionary prisms are very low stress-drop earthquakes. Geophysical Research Letters, 33.9.

Jibao, G., & Yaqian, Q., 1997. Hydrogen isotope fractionation and hydrogen diffusion in the tourmaline-water system. Geochimica et Cosmochimica Acta, v. 61, p. 4679-4688.

Johnson, K., Nissen, E., Saripalli, S., Arrowsmith, J. R., McGarey, P., Scharer, K., & Blisniuk, K., 2014. Rapid mapping of ultrafine fault zone topography with structure from motion. Geosphere, v. 10, p. 969-986.

Kerrich, R., & Allison, I., 1978. Vein geometry and hydrostatics during Yellowknife mineralisation. *Canadian Journal of Earth Sciences*, v. 15(10), p. 1653-1660.

Kerrick, D.M., 1970. Contact metamorphism in some areas of the Sierra Nevada, California. *Geological Society of America Bulletin*, v. 81, p. 2913-2938.

Kistler, R.W., Chappell, B.W., Peck, D.L., & Bateman, P. C., 1986. Isotopic variation in the Tuolumne intrusive suite, central Sierra Nevada, California. Contributions to Mineralogy and Petrology, v. 94, p. 205-220.

Lackey, J.S., Valley, J.W., Chen, J.H., & Stockli, D. F., 2008. Dynamic magma systems, crustal recycling, and alteration in the central Sierra Nevada batholith: the oxygen isotope record. Journal of Petrology, v. 49, p. 1397-1426.

Lerouge, C., & Bouchot, V., 2009. Conditions of formation and origin of fluids of quartz-tourmaline veins in the La Châtaigneraie tungstiferous district (Massif Central, France): fluid inclusions and stable isotopes. Bulletin de la Societe Geologique de France, v. 180, p. 263-270.

Lloyd, G.E., & Freeman, B., 1994. Dynamic recrystallization of quartz under greenschist conditions. Journal of Structural Geology, v. 16, p. 867-881.

Liu, Y., & Rice, J.R., 2005. Aseismic slip transients emerge spontaneously in three-dimensional rate and state modeling of subduction earthquake sequences. Journal of Geophysical Research: Solid Earth, 110(B8).

Magaritz, M., & Taylor, H. P., 1976. Oxygen, hydrogen and carbon isotope studies of the Franciscan formation, Coast Ranges, California. Geochimica et Cosmochimica Acta,v. 40, p. 215-234.

Matsuhisa, Y., Goldsmith, J.R., & Clayton, R.N., 1979. Oxygen isotopic fractionation in the system quartz-albite-anorthite-water. Geochimica et Cosmochimica Acta, v.43, p. 1131-1140.

Matsuzawa, T., Obara, K., & Maeda, T., 2009. Source duration of deep very low frequency earthquakes in western Shikoku, Japan. Journal of Geophysical Research: Solid Earth, 114(B11).

McCausland, W., S. Malone, *and* D. Johnson, 2005, Temporal and spatial occurrence of deep non-volcanic tremor: From Washington to northern California. Geophysical Research Letters, v. 32, L24311.

Memeti, V., Paterson, S.R., Putirka, K.D. (eds.), 2014. Formation of the Sierra Nevada Batholith: Magmatic and tectonic processes and their tempos, Field Guide 34. Geological Society of America, Boulder, 116 pp.

Micklethwaite, S., & Cox, S. F., 2004. Fault-segment rupture, aftershock-zone fluid flow, and mineralization. Geology, v. 32, p. 813-816.

Nokleberg, W.J., & Kistler, R.W., 1980. Paleozoic and Mesozoic deformations in the central Sierra Nevada. U.S. Geological Survey Professional Papers, 1145: 24 pp.

Nguyen, P.T., Cox, S.F., Harris, L.B. & Powell, C.M., 1998. Fault-valve behavior in optimally oriented shear zones: an example at the Revenge gold mine, Kambalda, Western Australia. Journal of Structural Geology, v. 20, p. 1625-1640.

Obara, K., 2002. Nonvolcanic deep tremor associated with subduction in southwest Japan. Science, v. 296, p. 1679-1681.

Obara, K., Hirose, H., Yamamizu, F., & Kasahara, K., 2004. Episodic slow slip events accompanied by non-volcanic tremors in southwest Japan subduction zone. Geophysical Research Letters, 31.23.

Passchier, C. W., & Trouw, R.A.J., 2005. Microtectonics. Springer Verlag, Berlin, Heidelberg, 366 pp.

Paterson, S.R., & Tobisch, O.T., 1992. Rates of processes in magmatic arcs: implications for the timing and nature of pluton emplacement and wall rock deformation. Journal of Structural Geology, v. 14, p. 291-300.

Paterson, S.R., Žak, J., & Janoušek, V., 2008. Growth of complex sheeted zones during recycling of older magmatic units into younger: Sawmill Canyon area, Tuolumne batholith, Sierra Nevada, California. Journal of Volcanology and Geothermal Research, v. 177, p. 457-484.

Peng, Z., Gomberg, J., 2010. An integrative perspective of coupled seismic and aseismic slow slip phenomena. Nature Geoscience, v. 3, p. 599-607.

Platt, J.P., & Behr, W.M., 2011. Grainsize evolution in ductile shear zones: Implications for strain localization and the strength of the lithosphere. Journal of Structural Geology, v. 33, p. 537-550.

La Rocca, M., Creager, K.C., Galluzzo, D., Malone, S., Vidale, J. E., Sweet, J. R., & Wech, A. G., 2009. Cascadia tremor located near plate interface constrained by S minus P wave times. Science, v. 323, p. 620-623.

Roedder, E., 1984. Fluid inclusions: Reviews in Mineralogy, v. 12, 644 pp.

Rogers, G., & Dragert, H., 2003. Episodic tremor and slip on the Cascadia subduction zone: The chatter of silent slip. Science, v. 300, p. 1942-1943.

Rubinstein, J.L., Vidale, J.E., Gomberg, J., Bodin, P., Creager, K. C., & Malone, S. D., 2007. Non-volcanic tremor driven by large transient shear stresses. Nature, v. 448, p. 579-582.

Rubinstein, J.L., Shelly, D.R., & Ellsworth, W.L., 2010. Non-volcanic tremor: A window into the roots of fault zones. In: *New Frontiers in Integrated Solid Earth Sciences,* ed. S Cloetingh, J Negendank, pp. 287-314. Dordrecht: Springer

Saleeby, J., 1981. Ocean floor accretion and volcanoplutonic arc evolution of the Mesozoic Sierra Nevada. In: W.G. Ernst (Editor), The Geotectonic Development of California: Rubey Volume I. Prentice-Hall, Englewood Cliffs, N.J. pp. 133-181.

Schweickert, R.A., & Cowan, D.S., 1975. Early Mesozoic tectonic evolution of the western Sierra Nevada, California. Geological Society of America Bulletin, v. 86, p. 1329-1336.

Schweickert, R.A., & Lahren, M. M., 2006. Geologic evolution of Saddlebag Lake pendant, eastern Sierra Nevada, California: Tectonic implications. Using stratigraphy, sedimentology, and geochemistry to unravel the geologic history of the southwestern Cordillera: Pacific Section, SEPM (Society for Sedimentary Geology), p. 27-56.

Schweickert, R.A., & Lahren, M.M., 1987. Continuation of Antler and Sonoma orogenic belts to the eastern Sierra Nevada, California, and Late Triassic thrusting in a compressional arc. Geology, v. 15, p. 270-273.

Schweickert, R.A., & Lahren, M.M., 1999. Triassic caldera at Tioga Pass, Yosemite National park, California: structural relationships and significance. Geological Society of America Bulletin, v. 111, p. 1714-1722.

Sharp, Z.D., 1990. A laser-based microanalytical method for the *in situ* determination of oxygen isotope ratios of silicates and oxides. Geochimica et Cosmochimica Acta, v. 54, p. 1353-1357.

Shea, W.T., & Kronenberg, A.K., 1993. Strength and anisotropy of foliated rocks with varied mica contents. Journal of Structural Geology, v. 15, p. 1097-1121.

Shelly, D.R., Beroza, G.C., Ide, S., & Nakamula, S., 2006. Low-frequency earthquakes in Shikoku, Japan, and their relationship to episodic tremor and slip. Nature, v. 442, p. 188-191.

Shelly, D.R., Beroza, G.C., & Ide, S., 2007. Non-volcanic tremor and low-frequency earthquake swarms. Nature, v. 446, p. 305-307.

Shelly, D.R., Beroza, G.C., & Ide, S., 2007. Complex evolution of transient slip derived from precise tremor locations in western Shikoku, Japan. Geochemistry, Geophysics, Geosystems, 8.10.

Shelly, D.R., 2015. Complexity of the deep San Andreas Fault zone defined by cascading tremor. Nature Geoscience.

Shelly, D.R., 2009, Possible deep fault slip preceding the 2004 Parkfield earthquake, inferred from detailed observations of tectonic tremor. Geophysical Research Letters, v. 36, L17318.

Shelly, D.R., & Hardebeck, J.L., 2010. Precise tremor source locations and amplitude variations along the lower-crustal central San Andreas Fault. Geophysical Research Letters, 37, L14301.

Sibson, R.H., 1975. Generation of pseudotachylyte by ancient seismic faulting. Geophysical Journal International, v. 43, p. 775-794.

Skarbek, R.M., Rempel, A.W., & Schmidt, D.A., 2012. Geologic heterogeneity can produce aseismic slip transients. Geophysical Research Letters, 39, L21306

Stevens, C.H., & Greene, D.C., 1999. Stratigraphy, depositional history, and tectonic evolution of Paleozoic continental-margin rocks in roof pendants of the eastern Sierra Nevada, California. Geological Society of America Bulletin, v. 111, p. 919-933.

Stipp, M., & Tullis, J., 2003. The recrystallized grain size piezometer for quartz. Geophysical Research Letters, 30.21.

Tikoff, B., & Greene, D., 1997. Stretching lineations in transpressional shear zones: an example from the Sierra Nevada Batholith, California. Journal of Structural Geology, v. 19, p. 29-39.

Thomas, A.M., Nadeau, R.M., & Bürgmann, R., 2009. Tremor-tide correlations and near-lithostatic pore pressure on the deep San Andreas fault. Nature, v. 462, p. 1048-1051.

Walsh, J.B., & Brace, W.F., 1964. A fracture criterion for brittle anisotropic rock. Journal of Geophysical Research, v. 69, p. 3449-3456.

Wech, A.G., Boese, C.M., Stern, T. A., & Townend, J., 2012. Tectonic tremor and deep slow slip on the Alpine Fault. Geophysical Research Letters, 39.10.

Wells, D.L., & Coppersmith, K.J., 1994. New Empirical Relationships among Magnitude, Rupture Length, Rupture Width, Rupture Area, and Surface Displacement. Bulletin of the Seismological Society of America, v. 84, p. 974-1002.

Williams, C.F., Grubb, F.V., & Galanis, S. P., 2004. Heat flow in the SAFOD pilot hole and implications for the strength of the San Andreas Fault. Geophysical Research Letters, 31, L15214.

Varga, R.J., & Moores, E. M., 1981. Age, origin, and significance of an unconformity that predates island-arc volcanism in the northern Sierra Nevada. Geology, v. 9, p. 512-518.

Žak, J. & Paterson, S.R., 2005. Characteristics of internal contacts in the Tuolumne Batholith, central Sierra Nevada, California (USA): Implications for episodic emplacement and physical processes in a continental arc magma chamber. Geological Society of America Bulletin, v. 117, p.1242-1255.

Zhang, J., Gerstoft, P., Shearer, P. M., Yao, H., Vidale, J. E., Houston, H., & Ghosh, A., 2011. Cascadia tremor spectra: Low corner frequencies and earthquake-like high-frequency falloff. Geochemistry, Geophysics, Geosystems, 12, Q10007.

Zheng, Y.F., Fu, B., Xiao, Y., Li, Y., & Gong, B., 1999. Hydrogen and oxygen isotope evidence for fluid–rock interactions in the stages of pre-and post-UHP metamorphism in the Dabie Mountains. Lithos, v. 46, p. 677-693.

# APPENDIX A

# EXPOSURE MAPS

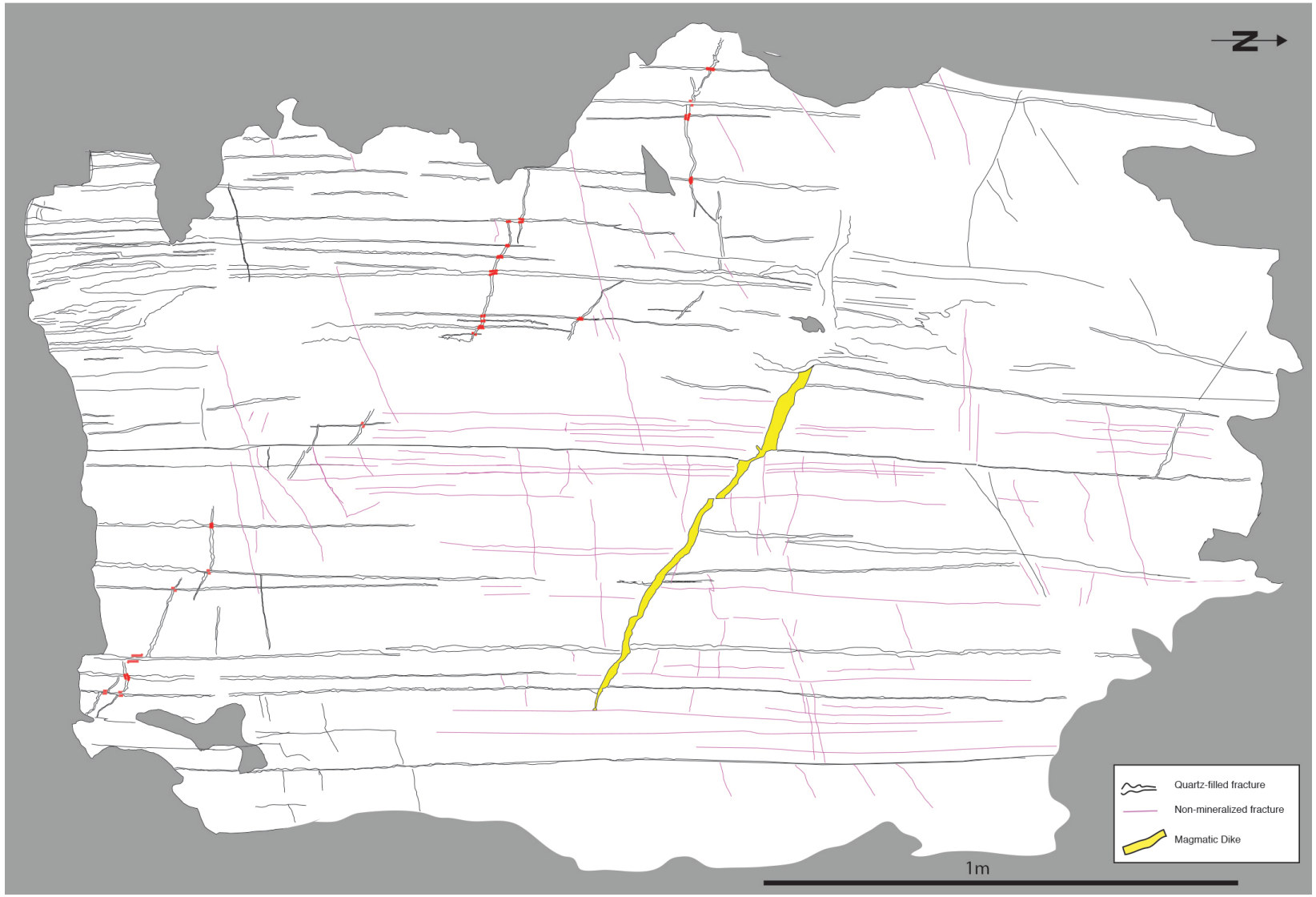


Figure 14 (previous page). Exposure map indicating amounts and orientations of quartz veins in a rhyolite outcrop. The base map was generated with Agisoft PhotoscanPro, and veins and fractures were mapped in the field. Red markers indicate crosscutting relationships between veins.

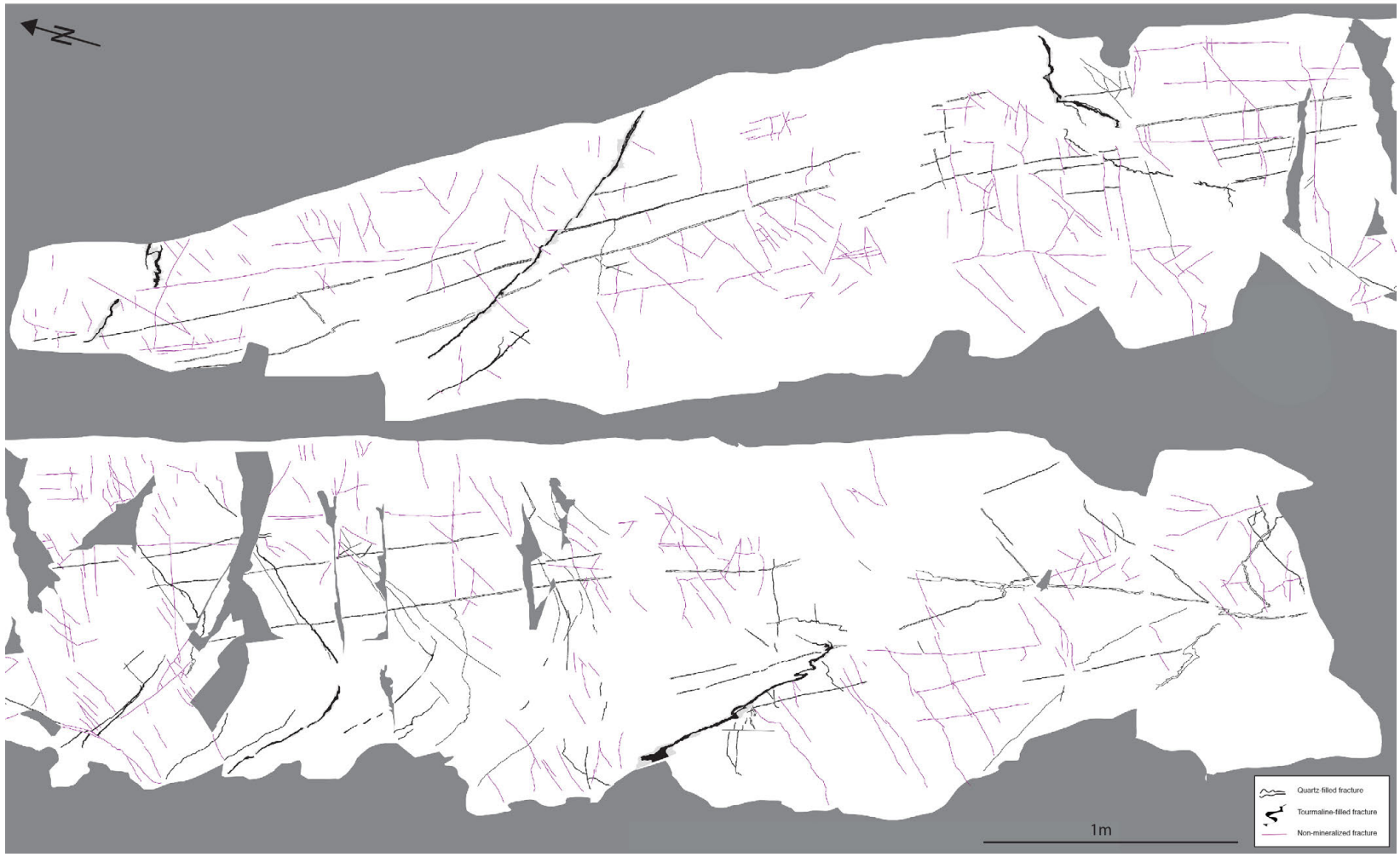


Figure 15. Exposure map of a Jurassic silicate metasedimentary outcrop. Outcrop map indicates quartz and tourmaline veins as well as fractures in a variety of orientations. Maps indicate the extent and amount of veins in an individual outcrop. Detailed crosscutting relationships indicate synkinematic brittle and ductile deformation.

# APPENDIX B

# FLUID INCLUSION THERMOBAROMETRY

Fluid inclusion analysis was conducted to collect homogenization and freezing temperatures to estimate trapping temperatures, (i.e. the temperatures at which the fluid inclusions originally cut the sample) of fluid inclusions. This process involves separating a doubly-polished thin section from the glass slide and using a liquid nitrogen stage to heat and cool the sample. A petrographic analysis of the fluid inclusions revealed two distinct sets of fluid inclusions, defined by different geometries and orientations. Further observation indicated the inclusions in my samples were of an aqueous, two-phase $H_2O$-NaCl system.

The homogenization temperature (Table 2) is measured by observing the temperature at which the fluid inclusion disappears from the sample; these temperatures are reached by heating the sample at a rate of ~10°/minute, slowing the rate to 1°C/minute around the expected homogenization temperatures.

First and final melting temperatures (Table 3) are reached by shock-freezing the sample to -100°C and heating it incrementally back to -30°C. Slow heating (1°C/minute) between -30°C and -21°C allows for observation of the first melting of a two- phase system (which the fluid inclusions in this study are). Slow heating (1°C/minute) between -7.0°C and 1.0°C allows for the observation of final melting in the same samples.

Freezing point depressions (final melting temperatures) of fluid inclusions are used to calculate the salinity of the fluid. Using the resulting salinity values and a pressure constrained by the depth of crystallization of the Sierra Nevada Batholith, (Žak and Paterson, 2005) trapping temperatures were calculated. These trapping temperatures are used to infer a temperature history of the system.

Table 2. Fluid inclusion homogenization temperatures.

| Sample | $T_h$ (°C) | Set 1/2 |
|---|---|---|
| 6A-1 | 244 | 2 |
| | 236 | 2 |
| | 220 | 2 |
| | 247 | 2 |
| | 243 | 2 |
| | 238 | 2 |
| | 245 | 2 |
| | 239 | 2 |
| | 245 | 2 |
| | 224 | 2 |
| | 222 | 2 |
| | 235 | 2 |
| | 241 | 2 |
| | 231 | 2 |
| | 243 | 2 |
| | 237 | 2 |
| | 275 | 1 |
| | 264 | 1 |
| | 274 | 1 |
| | 255 | 1 |
| | 290 | 1 |
| 6A-2 | 240 | 2 |
| | 246 | 2 |
| | 242 | 2 |
| | 233 | 2 |
| | 236 | 2 |
| | 231 | 2 |
| | 320 | 1 |
| | 360 | 1 |
| 6A-3 | 386 | 1 |
| | 380 | 1 |
| | 390 | 1 |
| | 287 | 2 |
| | 234 | 2 |
| | 385 | 1 |
| | 354 | 1 |
| | 393 | 1 |
| | 367 | 1 |
| | 340 | 1 |
| | 264 | 2 |
| | 260 | 2 |
| | 263 | 2 |
| | 270 | 2 |
| 6A-3 | 245 | 2 |
| | 236 | 2 |
| | 259 | 2 |
| | 267 | 2 |
| | 260 | 2 |
| 8A-1 | 250 | 2 |
| | 244 | 2 |
| | 268 | 2 |
| | 270 | 2 |
| | 265 | 2 |
| | 290 | 1 |
| | 298 | 1 |
| | 316 | 1 |
| | 254 | 2 |
| | 245 | 2 |
| | 268 | 2 |
| | 243 | 2 |
| | 321 | 1 |
| | 335 | 1 |
| | 358 | 1 |
| | 362 | 1 |
| 8A-2 | 234 | 2 |
| | 241 | 2 |
| | 261 | 2 |
| | 265 | 2 |
| | 285 | 2 |
| | 382 | 1 |
| | 376 | 1 |
| | 351 | 1 |
| | 410 | 1 |
| 8A-3 | 355 | 1 |
| | 357 | 1 |
| | 362 | 1 |
| | 368 | 1 |
| | 360 | 1 |
| | 357 | 1 |
| | 387 | 1 |
| | 361 | 1 |
| | 370 | 1 |
| | 412 | 1 |
| | 401 | 1 |
| | 398 | 1 |
| 15A-1 | 259 | 2 |
| | 263 | 2 |
| | 334 | 1 |
| | 364 | 1 |
| | 321 | 1 |
| | 343 | 1 |
| | 361 | 1 |
| | 366 | 1 |
| | 255 | 2 |
| 16A-1 | 290 | 1 |
| | 241 | 2 |
| | 250 | 2 |
| | 324 | 1 |
| | 281 | 2 |

Table 3. Fluid inclusion first ($T_{eutectic}$) and final ($T_{ice}$) melting temperatures.

| Sample | $T_{eutectic}$ (°C) | $T_{ice}$ (°C) | Set 1/2 |
|---|---|---|---|
| 6A-1 | -25.1 | -1.9 | 2 |
| | -22.9 | -1.7 | 2 |
| | -23.5 | -2.1 | 1 |
| | -24.6 | -1.2 | 2 |
| | -25.2 | -2.5 | 1 |
| 8A-1 | -24.8 | -1.8 | 1 |
| | -24 | -1.6 | 2 |
| | -22.6 | -2.0 | 1 |
| | -25.5 | -2.5 | 1 |
| 16A-1 | -26.1 | -1.1 | 2 |
| | -26.4 | -1.6 | 2 |
| | -24.7 | -1.2 | 2 |

# APPENDIX C

# TOURMALINE VEIN MOSAIC

Figure 16. Photomosaic of photomicrographs taken from a thin section of a tourmaline vein express the nature of the quartz lenses included within the tourmaline. Quartz lenses are observed in the middle of the tourmaline vein and are folded with the vein. Because of this, we interpret they formed as a result of a later pulse of meteoric fluid (supported by isotopic data)